Breakup of a laminar liquid jet by coaxial non-swirling and swirling air streams

Breakup of a laminar liquid jet by coaxial non-swirling and swirling air streams

Yifan Liang,[1] Lars Christian Johansen,[1] and Mark Linne[1]
Institute for Multiscale Thermofluids, School of Engineering, University of Edinburgh, James Clerk Maxwell Building, Peter Guthrie Tait Road, Edinburgh, EH9 3FD, United Kingdom

(*Electronic mail: yifan.liang@ed.ac.uk)

(Dated: 15 August 2022)

This paper describes an experimental study on shear-based spray formation. A laminar liquid jet was ejected inside co-annular non-swirling and swirling air streams. The aerodynamic Weber numbers (We_A) and swirl numbers (S) of the flow cases ranged from 4 to 1426 and from 0 to 3.9, respectively. High-speed shadowgraphy was utilised to obtain data on the first droplet locations, breakup lengths of the liquid jets, and two-dimensional wave spatiotemporal spectra for the jets. In order to detect the large-scale instabilities of the central liquid jet, proper orthogonal decomposition (POD) was performed on the high-speed shadowgraphic images. Stereo particle image velocimetry (SPIV) was utilised to investigate the annular air flow fields with S in the range of $0-2.5$. It was found that air swirl promotes the morphological development of the jets with S in the range of $1.2-2.5$. Both the breakup length and axial distance between the first droplet separation and the nozzle exit reduce as We_A and S increase. Scaling of the first droplet locations and breakup lengths is also evaluated in this paper. In terms of the air flow fields, radial expansion of the annular swirling air jets was observed, and the annular swirling jets expand radially further as S goes up. Central reversal air flows appear near the nozzle exit when $S \geq 1.2$, and some small droplets are blown upwards to the nozzle exit by these central reversal air flows. In terms of large-scale instabilities, flapping is the dominant instability across most of the flow cases (as revealed by the first POD mode). Wavy and explosive breakup appear as the secondary breakup modes when We_A is low (≤ 110). In the absence of the central reversal air flows, the temporal frequencies of the instabilities of the air-water interfaces increase as S goes up. It was found that the central reversal air flows tend to stabilize the air-water interfaces. The spatial frequencies of the instabilities of the air-water interfaces remain low (≤ 0.06 mm^{-1}) across all the flow cases which produce long wave structures.

I. INTRODUCTION

Spray systems are widely used in many applications such as fuel injection for internal combustion engines, for coating surfaces, and drug delivery to human air passages, for example. Sprays are produced by an atomizer, among which there are many types (pressure, rotary, air-assist, air blast atomizers, etc.)[1]. A liquid jet will undergo a pressure drop as it leaves a nozzle, and then break into drops and ligaments during the atomization process[2]. The size and velocity distributions of the droplets play a key role in spray system performance. Unfortunately, there is currently no fully predictive model for realistic spray formation owing to the lack of detailed spray formation statistics to be used for model validation. In general, there are three major breakup mechanisms, including: turbulence in the liquid, aerodynamic forces acting on the gas-liquid interface (also called "shear forces"), and cavitation inside the nozzle[1]. Hence, in order to develop a validation database for research groups in computational fluid dynamics (CFD), each of these breakup mechanisms should be isolated from the others and a complete validation dataset obtained. Otherwise, atomization might be simultaneously caused by interaction of these three breakup mechanisms, which will make CFD validation more difficult and uncertain. The aim of the program described in this paper (and others to follow) is to develop a comprehensive database for the spray formation caused by shear forces alone. A database containing these results has been prepared and it is available to interested parties[3]. In this paper, spray morphology, breakup lengths, axial location of first droplet formation, large-scale, shear instabilities and air flow fields are reported and analyzed.

Breakup length is one of the most important characteristics of a co-annular non-swirling jet. The breakup length of the liquid jet is related to the gas-to-liquid momentum flux ratio (M) . When $M \ll 1$, the breakup length is determined by the liquid jet[4]. On the other hand, when $M \gg 1$, the breakup length depends more on the gas jet[5,6]. If M exceeds the critical momentum flux ratio M_c (of about 50), a gas cavity can be formed by the recirculating gas motion downstream of the liquid core. This gas cavity breaks the liquid core, and the breakup length becomes very short[7]. Although a lot of research on the breakup lengths of co-annular non-swirling jets has been done[8–11], only a handful of studies on the breakup lengths of the co-annular swirling jets have been reported. Kumar and Sahu [12] obtained an empirical correlation for the turbulent liquid breakup length in a co-annular swirling jet. Machicoane *et al.* [13] measured the breakup length of a laminar water jet in a co-annular air jet with swirl (S, see Eq. 4) in the range of $\sim 0-1$. They found that the liquid core length average and standard deviation decrease as M and S increase. Dunand, Carreau, and Roger [14] used a phase Doppler analyzer (PDA), tomography, and an optical fiber probe to investigate the breakup of a central turbulent water jet by a co-annular swirling air jet. They found that a hollow-cone spray appears when the gas swirl number goes beyond the critical swirl number of their nozzle. Furthermore, a transition to "explosive breakup" of the liquid jet (caused by a gas-phase recirculation zone) significantly reduces the breakup length[14]. They also found that the addition of the annular swirling gas stream re-

duces the breakup length of the liquid jet more significantly as the momentum ratio grows. Hopfinger and Lasheras [5] and Hardalupas and Whitelaw [15] found that the addition of a swirling annular gas stream has a significant effect on the breakup of the turbulent liquid jet if the swirl number goes beyond the critical swirl number. When the swirl number is above the critical swirl number (S_{cr}), a central recirculating flow and a stagnation point on the centreline of the liquid jet axis can be observed. Hopfinger and Lasheras [5] found a relationship between the critical swirl number and the gas to liquid momentum flux ratio. The relationships between the laminar liquid breakup lengths and the aerodynamic Weber numbers when $S > 1$ remain unknown and are investigated in this present study. A comprehensive database for spray formation should include the first droplet location data which has not been investigated in prior work. Hence, the relationships between the first droplet locations and aerodynamic Weber numbers and swirl numbers are investigated in this paper.

Apart from breakup length, shear instability is one of the most important characteristics of a coaxial jet. It can be observed on the gas-liquid interface because the aerodynamic forces from the gas act on the liquid jet. Matas, Delon, and Cartellier [16] and Kumar and Sahu [11] investigated shear instabilities in coaxial non-swirling jets. In order to measure the shear instability frequency, they performed a fast Fourier transform (FFT) on the temporal signal measuring height of the air-water interface and obtained the frequency spectra of shear instabilities. They found that the temporal frequency goes up as the coflowing gas velocity increases, indicating that an increase in the aerodynamic forces destabilizes the liquid-gas interface more significantly. However, how air swirl affects the spatial and temporal shear instability spectra remains unknown and is a topic of this paper.

In order to understand how air swirl influences the large-scale instabilities of the co-annular swirling and non-swirling jets, Kumar and Sahu [17] used high-speed shadowgraphy and POD (proper orthogonal decomposition) to investigate a central turbulent water jet surrounded by a co-annular air flow, with and without swirl, over a wide range of aerodynamic Weber numbers, $We_A(80-958)$, momentum ratios, $M(1-26)$, and swirl numbers, $S(0-1.6)$. Based on the extracted POD modes, they found three types of large-scale instabilities, including: jet flapping, wavy or sinuous breakup, and explosive breakup, over a wide range of liquid and gas conditions. Kumar and Sahu [17] developed regime maps characterized by swirl number and momentum ratio for co-annular swirling jets. They found that the strength of the air swirl makes a small difference in the development of the wavy breakup instability. However, air swirl enhances explosive breakup instability because increasing the strength of the air swirl strengthens air recirculation. In addition, in order to understand how the strength of the air swirl influences the Kelvin-Helmholtz instability near the nozzle exit, Kumar and Sahu [17] measured the radius of the air-water interface at a downstream position one-fourth of the liquid tube diameter, at various swirl numbers, performed FFT on that temporal signal, and obtained the temporal frequency of the Kelvin-Helmholtz instability driven by the shear forces at the air-water interface. They found that increasing the strength of the air swirl results in an increase in the temporal frequency, especially when the aerodynamic Weber number is large. However, how the temporal frequency and large-scale instability of a coaxial swirling jet change when its swirl number goes beyond 1.6 has not been explored until now.

Litvinov, Sharaborin, and Shtork [18] used stereoscopic particle image velocimetry (SPIV) to investigate the velocity vector field near the outlet of a tangential air swirler. A co-annular swirling air jet around a central air jet was investigated by Rajamanickam and Saptarshi [19] using two-dimensional particle image velocimetry (PIV). However, the motion of the annular gas streams of the coaxial non-swirling and swirling liquid-gas jets remains unknown. In this paper, SPIV is used to investigate the velocity vector fields of the coaxial swirling and non-swirling jets.

Although Lasheras and Hopfinger [7] established the regime map characterised by the liquid Reynolds number and aerodynamic Weber number, how the strength of the air swirl influences the morphological development of the breakup regimes remains unknown and is explored in this paper. Although the research discussed above has been done on the breakup of a central turbulent liquid jet surrounded by a co-annular air flow with and without swirl, the breakup of a central laminar liquid jet surrounded by a co-annular air flow with and without swirl remains unknown and is investigated in this paper. It is our view that the use of a laminar liquid jet simplifies model validation. The effects of the strength of the air swirl and the aerodynamic forces on the first droplet locations and 2D shear instability spectra remain unknown and are explored in this paper. Although Machicoane *et al.* [13] measured the breakup length of the laminar water jet in a co-annular air jet with S in the range of $\sim 0-1$, the relationships between the laminar liquid breakup lengths and the aerodynamic Weber numbers when $1 < S \leq 3.9$ remain unknown and are investigated in this present study. Although Kumar and Sahu [17] investigated large-scale instabilities of a central turbulent water jet surrounded by a co-annular air flow with S in the range of $\sim 0-1.6$, large-scale instabilities of a central laminar water jet surrounded by a co-annular air flow with S in the range of $\sim 0-3.9$ were investigated in this paper. There is a dearth of information on the motion of the co-annular air flows near the nozzle exit, which is investigated using SPIV in this paper.

This paper is organized as follows. Section II describes the experimental setup and procedure. Section IV shows the result of the morphological study, the scaling of the breakup length and first droplet location data, POD and 2D FFT analyses, and SPIV measurements. Section V presents conclusions of the work.

II. EXPERIMENTAL SETUP AND PROCEDURE

A. Overall Setup

Two mass flow controllers (MFC) (Bronkhorst Inc) are used to control and measure the air and water flow rates. The central liquid jet and annular gas stream are water and air respec-

tively (see Fig. 1). The inner diameters of the liquid and co-flow tubes are 4 mm and 10 mm, respectively. The outer diameters of the liquid and co-flow tubes are 5 mm and 14 mm, respectively. Air enters the air chamber through an inlet located at the bottom of the chamber. Then it flows through an air filter to render the nozzle in-flow azimuthally uniform, and it subsequently enters the co-flow tube (see Fig. 1a and Fig. 1b). In order to introduce swirl into the air, a swirler is added to the inner surface of the co-flow tube (see Fig. 1c). The circular gap between the air swirler and the water tube is sealed with an O ring to avoid air leakage. There are eight types of air swirlers with different vane angles. All the air swirlers have a four-star shape. The cross-sectional areas of the air outlets with and without the air swirler are 28.09 mm^2 and 58.9 mm^2, respectively. The lengths of the water tubes and co-flow tubes are 140 mm and 43 mm, respectively. Further detail regarding the experiment can be found in Liang, Johansen, and Linne [3]. The Reynolds number of the central water jet is kept at 480 for all the flow cases to ensure that the laminar pipe flow becomes fully developed before it leaves the nozzle exit. In the absence of significant shear, a fully developed parabolic velocity profile evolves into a flat velocity profile when the liquid jet leaves the nozzle[1]. The energy within the liquid jet redistributes simultaneously, which is thought by some to cause bursting breakup[1,20]. Ibrahim and Marshall [21] found that the effects of the parabolic velocity profile relaxation on jet instability are weaker than the flat velocity profile relaxation. In this work, it was observed that in the absence of the co-annular air flows there is no contribution to the breakup of the central water jet from velocity profile relaxation.

B. Operating Conditions for the Atomizer

The characteristics of twin-fluid atomization, such as the first droplet location, jet instability and breakup length of the liquid jet, are related to the fluid material properties and the relative velocities between those two fluids. In this work, three non-dimensional parameters were used to describe the operating conditions of the twin-fluid atomizer. They are the aerodynamic Weber number (We_A, the ratio of the aerodynamic forces to the liquid surface tension forces), the liquid Reynolds number (Re_l, the ratio of the liquid inertial forces to viscous forces), and the gas to liquid momentum flux ratio (M). They are given by:

$$We_A = \frac{\rho_g (U_g - U_l)^2 D_l}{\sigma_l}, \tag{1}$$

$$Re_l = \frac{U_l D_l}{\nu_l}, \tag{2}$$

$$M = \frac{\rho_g U_g^2}{\rho_l U_l^2}. \tag{3}$$

Here, ρ_l is the density of the liquid, ρ_g is the density of the gas, U_g is the gas velocity, U_l is the liquid velocity, D_l is the diameter of the liquid tube, σ_l is the surface tension of the liquid, and ν_l is the kinematic viscosity of the liquid. Additiona-

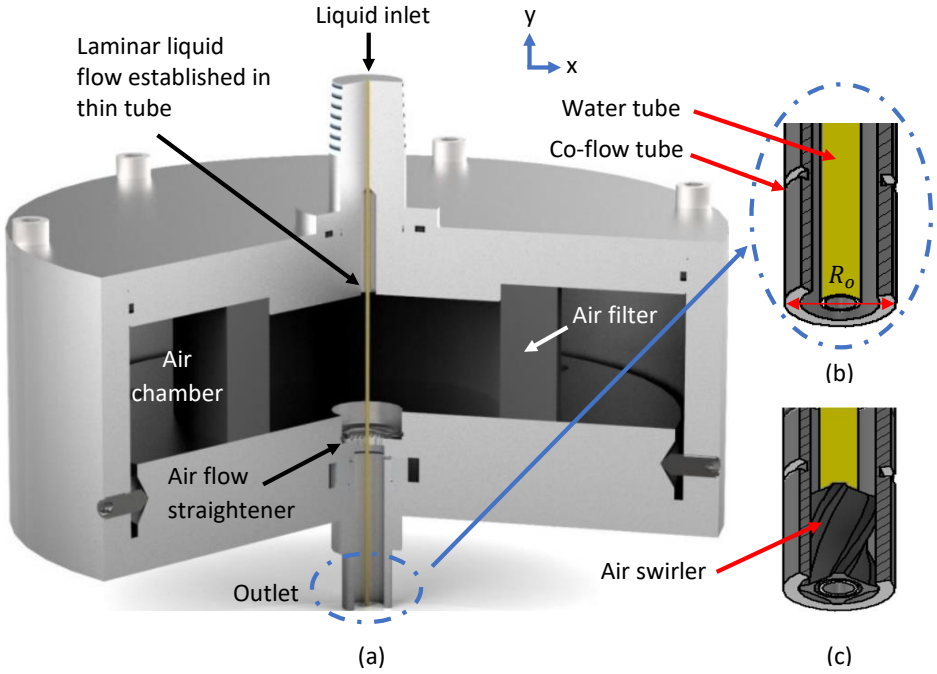

FIG. 1: (a) Atomizer. (b) Broken-out view of the co-flow tube without air swirler attached on it. (c) Broken-out view of the co-flow tube with the air swirler.

TABLE I: Comparisons between the geometrical and actual swirl numbers.

S[a]	S_{meas}[b]
0.3	0.1
0.8	0.3
1.2	0.5
1.5	0.7
2.5	1.3

[a] Geometrical swirl number
[b] Measured swirl number

lly, the swirl number (S), which is the ratio of the axial flux of swirl momentum to axial flux of axial momentum, is generally used to describe the operating conditions of a swirling flow. According to Giannadakis, Perrakis, and Panidis [22] and Ivanic, Foucault, and Pecheux [23], it is given by:

$$S = \frac{\int_0^\infty U_y U_\theta r^2 \, dr}{R_O \int_0^\infty U_y^2 r \, dr}, \tag{4}$$

where U_y is the axial velocity, U_θ is the tangential velocity and R_O is the outer radius of the co-flow tube (see Fig. 1b). The correlations for geometrical swirl numbers depend on the type of the air swirler. Details can be found in Giannadakis, Perrakis, and Panidis [22]. According to Hardalupas and Whitelaw [15], based on the type of the air swirler used in this project, the geometrical swirl number is given by,

$$S = \frac{2}{3} \tan\theta \frac{1 - \left(\frac{D_O}{D_G}\right)^3}{1 - \left(\frac{D_O}{D_G}\right)^2}, \tag{5}$$

where θ is the swirl vane angle, D_0 is the external diameter of the liquid tube, and D_G is the diameter of the vane pack hub. Table I shows a comparison between the geometrical and measured swirl numbers. Note that the measured swirl numbers (S_{meas}) were calculated based on the SPIV data (the approach to calculate S_{meas}, and the differences between S_{meas} and S are discussed in detail in Sec. IV C). Note that in this work, the geometrical swirl numbers (S) were used to describe the operating conditions of the atomizer. For simplicity, the term "swirl number" mentioned throughout the sections of this work refers to the "geometrical swirl number".

The operating conditions of the atomizer are shown in Tables II and III. In this work, three independent samplings of the data were collected for each operating condition shown in Table II. A morphological study was performed on the operating conditions shown in Tables II and III (the morphological study is discussed in more detail in Sec. IV A). The operating conditions shown in Table III were investigated using different techniques and they are discussed in more detail in a different paper[24]. The magnitudes of We_A in the tables were chosen based on the rule that the operating conditions under each swirl number should include various types of breakup regimes. It should also be noted that U_l and U_g are the axial bulk velocities of the liquid jet and gas stream at the nozzle exit, respectively. The critical swirl number for our nozzle is equal to 0.8 (following Hopfinger and Lasheras [5]).

TABLE II: Operating conditions for the atomizer. FWI: first-wind induced; SWI: second-wind induced; B: bag breakup regime.

Case	$\dot{m}_g$ (kg/h)	We_A	M	S	Breakup regime	U_l (m/s)	Re_l
1	3	9	14		FWI		
2	4	16	24		SWI		
3	5	25	38	0	B		
4	8	64	96		B		
5	10	100	150		B		
6	3	40	60		SWI		
7	6	158	237	0.3	B		
8	8	282	423		B		
9	10	440	660		B		
10	3	40	60		SWI		
11	6	158	237	0.8	B		
12	8	282	423		B		
13	10	440	660		B		
14	3	40	60		SWI		
15	5.5	133	200	1.2	B		
16	8	282	423		B		
17	10	440	660		B	0.11	438
18	2	18	27		B		
19	3	40	60	1.5	B		
20	4	70	105		B		
21	5	110	165		B		
22	1.5	10	15		B		
23	1.8	14.3	21	2.5	B		
24	2	18	27		B		
25	3	40	60		B		
26	1	4	7		B		
27	1.3	7	11	3.1	B		
28	2	18	27		B		
29	3	40	60		B		
30	1	4	7		SWI		
31	2	18	27	3.9	B		
32	3	40	60		B		

C. Experimental Procedure

For high-speed shadowgraphy, a Phantom VEO 710L high-speed camera acquired images of the swirling and non-swirling jets. The spatial resolution was around 140 μm/pixel and the exposure time was about 10 μs. As mentioned in Sec. II B, three independent samplings of the data were collected for each operating condition shown in Table II. Thresholding was applied to each image under the associated operating conditions. The first droplet locations and the breakup lengths of the liquid jets under various operation conditions were detected using image processing in Matlab. Furthermore, based on the high-speed images, the interface positions were captured at many different moments in time using image processing in Matlab, and a two-dimensional FFT was performed on the data (the approach is described in more detail in Sec. III B). POD was also performed on these high-speed

TABLE III: Operating conditions for the atomizer. B: bag breakup regime; F: fiber-type atomization; BF: boundary of fiber-type atomization.

Case	$\dot{m}_g$ (kg/h)	We_A	M	S	Breakup regime	U_l (m/s)	Re_l
33	16	256	384	0	B	0.11	438
34	18	324	486				
35	16	1126	1689	0.3			
36	18	1426	2139				
37	16	1126	1689	0.8	B		
38	18	1426	2139		BF		
39	16	1126	1689	1.2	B		
40	18	1426	2139		BF		
41	8	282	423	1.5	F		
42	10	440	660				
43	8	282	423	2.5			
44	10	440	660				
45	8	282	423	3.1			
46	10	440	660				
47	8	282	423	3.9			
48	10	440	660				

images, to find the dominant large-scale instability modes of the liquid jets (the approach is described in more detail in Sec. III A). The corresponding temporal frequencies of these modes were also obtained by performing FFT on the corresponding columns of the matrix $\boldsymbol{V}$ that contains the temporal patterns of the data[25]. The uncertainties of the breakup length and first droplet location data for each flow case, originating in the spatial resolution, thresholding level, and recording time duration, were evaluated. It was found that the uncertainties of the data caused by these factors are relatively small (of the order of 5%). The uncertainties in the POD data, caused by the spatial resolution and sampling frequency, were evaluated. It was found that the uncertainties of the data are relatively small (of the order of 3%). Furthermore, the periods and temporal frequencies of the large-scale instabilities are much smaller than the sampling time durations and frequencies, respectively.

SPIV was used to measure the air flow fields without the presence of the central water jet. For SPIV, each camera took 100 images for each flow case. The average results were obtained using all 100 images. For most of the flow cases, after being removed by the median and peak ratio filters (these filters are described in more detail in Sec. II D), the number of the source vectors at each grid to compute the average value was above 80. However, there were few high-swirl flow cases where the number of the source vectors at some grids near the nozzle exit was 55. This can be explained by the fact that the narrow air passages of the air swirlers with high swirl numbers result in low particle density near the nozzle exit. The number of the source vectors at each grid for all the flow cases can be found in the database[3].

D. Stereoscopic Particle Image Velocimetry (SPIV)

In terms of the SPIV setup, 3.5 μm graphite particles were used as the seeding material, with a Stokes number much less than 1. A 10 Hz dual-pulse Nd: YAG laser (Quantel Inc.) at a wavelength of 532 nm was used to illuminate the seeding particles. Two Phantom VEO 710L cameras with Scheimpflug mounts acquired images of the swirling and non-swirling air jets (see Fig. 2). The image resolution was 895 pixel$\times$1283 pixel, with a spatial resolution of 12.15 pixel/mm. The angle between the optical axes of these two cameras was 78°, which was obtained from the calibration in Davis 10.2 software (Lavision Inc). A cylindrical concave lens was used to diverge the laser beam vertically. The laser sheet thickness at the jet center-line was 2.1 mm, as measured by a WinCamD (DataRay Inc). The laser sheet was aligned with the center of the nozzle exit (see Fig. 3). A programming timing unit (PTU, Lavision Inc) was used to synchronize the laser and the two cameras. The double-frame raw images were processed using Davis 10.2. Cross-correlation and multi-pass, with reducing interrogation window size, were used to calculate 2D vector fields for each camera. For each pass, the corresponding 2D vectors from two cameras were combined to reconstruct the 3D vectors. The corresponding 2D vector components were removed if their stereo errors were larger than 1 (the definition of the stereo error can be found in the manual of Lavision[26]). After that, the peak ratio ($Q > 1.5$) and median filters were applied to the 2D vector fields to remove spurious vectors. The 2D vector components (U, V) were removed by the median filter if their values did not satisfy the following rules: $U_{\text{median}} - 3 \times U_{\text{deviation}} < U < U_{\text{median}} + 3 \times U_{\text{deviation}}$ and $V_{\text{median}} - 3 \times V_{\text{deviation}} < V < V_{\text{median}} + 3 \times V_{\text{deviation}}$. The new candidates corresponding to the second, third or fourth correlation peak would be reinserted if they satisfied the rule that $U_{\text{median}} - 2 \times U_{\text{deviation}} < U < U_{\text{median}} + 2 \times U_{\text{deviation}}$ and $V_{\text{median}} - 2 \times V_{\text{deviation}} < V < V_{\text{median}} + 2 \times V_{\text{deviation}}$. For each camera, the final interrogation window size was 32 pixel $\times$ 32 pixel. The overlap ratio of the interrogation windows was 75%. For each flow case, the time between pulses was determined by the rule that the maximum particle displacement should be less than one-fourth of the interrogation window size.

III. DATA ANALYSIS METHODS

A. Proper Orthogonal Decomposition (POD)

In this work, proper orthogonal decomposition (POD) was applied to the jet shadowgrams. POD is a matrix factorization method and can decompose a rectangular data matrix, consisting of scalar or vector fields, into a set of rank 1 matrices, referred to as modes or principal components, ordered in terms of the data matrix covariance eigenvalues[27]. When the data are a velocity field, the eigenvalues correspond to kinetic energy. POD is more generally known as principal component analysis[27,28]. The total number of POD modes or principal components is equal to the rank of the data matrix[29]. Each

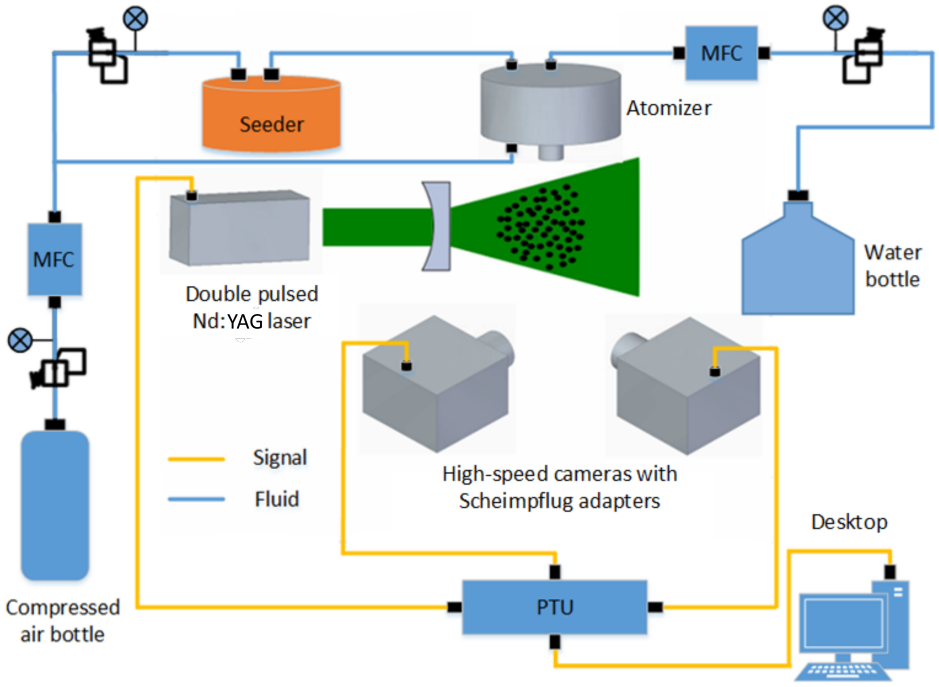

FIG. 2: SPIV setup.

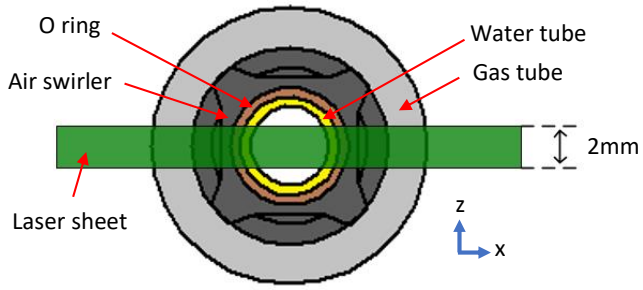

FIG. 3: Bottom view of the nozzle exit with the laser sheet.

POD mode corresponds to a singular value of the data matrix, and the relative magnitude of the singular value indicates how closely the mode approximates the original data matrix[28]. Generally, there are two ways to perform POD on fluid flow data; spatial (classical) POD and snapshot POD. The spatial POD can be determined using the singular value decomposition (SVD)[27]. More details about the spatial POD method and snapshot POD method can be found in Taira *et al.*[27]. Spatial POD was used to analyse the shadowgram images of the jet in this work. Spatial POD using the SVD is described in this section.

Each shadowgram image of the jet can be represented as a matrix $\boldsymbol{D} \in \mathbb{R}^{p\times q}$ with each entry d_{ij} corresponding to a spatial coordinate:

$$d_{ij} = k\left(\xi_i, \eta_j\right), \tag{6}$$

where k is a function over the spatial coordinates ξ_i and η_j. The shadowgram matrix $\boldsymbol{D}\left(t_k\right)$ for each image taken at time t_k is rearranged as a column vector $\boldsymbol{x}\left(t_k\right)$. There is no unique mapping between the image matrix $\boldsymbol{D}\left(t_k\right)$ and the image column vector $\boldsymbol{x}\left(t_k\right)$. The mapping used in the present work is given here as an example:

$$\boldsymbol{x}\left(t_k\right) = \begin{bmatrix} d_{1,1}\left(t_k\right) \\ d_{2,1}\left(t_k\right) \\ \vdots \\ d_{1,2}\left(t_k\right) \\ \vdots \\ d_{p,q}\left(t_k\right) \end{bmatrix} \tag{7}$$

The set of column vectors $\boldsymbol{x}\left(t_k\right)$ forms a matrix $\boldsymbol{X}$ given by:

$$\boldsymbol{X} = \left[\boldsymbol{x}\left(t_1\right), \boldsymbol{x}\left(t_2\right), \boldsymbol{x}\left(t_3\right), \ldots, \boldsymbol{x}\left(t_m\right)\right] \in \mathbb{R}^{n\times m}, \tag{8}$$

where $n = p \times q$ is the number of spatial coordinates, and m is the number of the measurement times. Note that the data vectors should be placed in order of time at which each image was taken. Each row of $\boldsymbol{X}$ corresponds to a two-dimensional spatial coordinate and each column corresponds to a time. The mean value of each row of the matrix $\boldsymbol{X}$ is subtracted from $\boldsymbol{X}$ which provides the data matrix $\boldsymbol{K}\left(\zeta, t\right)$ containing the components of $\boldsymbol{X}\left(\zeta, t\right)$ which vary with time:

$$\boldsymbol{K}\left(\zeta, t\right) = \boldsymbol{X}\left(\zeta, t\right) - \overline{\boldsymbol{X}\left(\zeta\right)}, \tag{9}$$

where, ζ denotes the spatial coordinate and $\overline{\boldsymbol{X}\left(\zeta\right)}$ is the matrix that contains the mean value of each row of the scalar field $\boldsymbol{X}\left(\zeta, t\right)$, in each column. Note that the matrix $\boldsymbol{X}$ is written as $\boldsymbol{X}\left(\zeta, t\right)$ in equation 9 to emphasize that the data are collected from the two-dimensional grid at discrete moments t.

According to Strang [29], the reduced SVD decomposition of the n by m matrix $\boldsymbol{K}$ is given by:

$$\boldsymbol{K} = \boldsymbol{U}\boldsymbol{\Sigma}\boldsymbol{V}^T = [\boldsymbol{u}_1, \boldsymbol{u}_2, \ldots, \boldsymbol{u}_r] \begin{bmatrix} \sigma_1 & 0 & \ldots & 0 \\ 0 & \sigma_2 & \ldots & 0 \\ \vdots & \vdots & \ddots & \vdots \\ 0 & 0 & 0 & \sigma_r \end{bmatrix} \begin{bmatrix} \boldsymbol{v}_1^T \\ \boldsymbol{v}_2^T \\ \vdots \\ \boldsymbol{v}_r^T \end{bmatrix}$$
$$= \boldsymbol{u}_1\sigma_1\boldsymbol{v}_1^T + \boldsymbol{u}_2\sigma_2\boldsymbol{v}_2^T + \ldots + \boldsymbol{u}_r\sigma_r\boldsymbol{v}_r^T, \quad (10)$$
$$\boldsymbol{U} \in \mathbb{R}^{n\times r}, \boldsymbol{V} \in \mathbb{R}^{m\times r}, \boldsymbol{\Sigma} \in \mathbb{R}^{r\times r}, \sigma_1 \geq \sigma_2 \geq \ldots \geq \sigma_r > 0,$$

where, r is the rank of the matrix $\boldsymbol{K}$, $\sigma_i, i = 1,2,...,r$, denote singular values, the superscript T denotes transpose, and $\boldsymbol{u}_i, \boldsymbol{v}_i, i = 1,2,...,r$ are called left singular vectors and right singular vectors, respectively[29]. $\boldsymbol{u}_i, i = 1,2,...,r$, are also called the POD modes[27]. It should be noted that the matrices $\boldsymbol{U}$ and $\boldsymbol{V}$ are orthonormal, which means that:

$$\boldsymbol{U}^T\boldsymbol{U} = \boldsymbol{V}^T\boldsymbol{V} = \boldsymbol{I}_{r\times r}, \quad (11)$$

where $\boldsymbol{I}$ denotes the identity matrix. Each POD mode $\boldsymbol{u}_i$ is therefore orthonormal to any other mode $\boldsymbol{u}_{j\neq i}$ and forms a linearly independent set. The same is true for $\boldsymbol{v}_i$.

The left singular vectors, or POD modes, $\boldsymbol{u}_i$ contain the spatial components of $\boldsymbol{K}$. The right singular vectors $\boldsymbol{v}_i$ contain the temporal components. Performing a Fourier transform on the matrix $\boldsymbol{V}$ obtained from SVD yields the frequency of each mode. The left singular vector $\boldsymbol{u}_i$ for each mode can be rearranged into a matrix with dimension $q \times p$, the same dimensions as the shadowgram image matrices $\boldsymbol{D}$, for visualization of the POD modes.

B. Two-dimensional Fast Fourier Transform (2D FFT)

In this work, the left-hand-side air-water interface locations were captured at many different moments in time, and a two-dimensional FFT was performed on the data to obtain the temporal and spatial frequencies of the shear instabilities. The algorithm is explained as follows. For each operating condition, a group of shadowgrams was captured by the high-speed camera, and the minimum breakup length and interface locations were detected using Matlab. All the interface location data were truncated to the same length, which was equivalent to the minimum breakup length, before they were imported into a data matrix. The data matrix was organized so that each column represented the interface locations at different axial positions and a specific moment in time, while each row represented the interface locations at a fixed axial position and different moments. After that, the mean value of the data matrix was subtracted from the matrix. A 2D FFT was then performed on this data matrix to obtain the spatial and temporal frequencies of the shear instabilities on the left-hand-side air-water interfaces. The periods and temporal frequencies of the shear instabilities were much smaller than the sampling time durations and frequencies, respectively. The uncertainties of the wave spectra caused by the sampling time duration were evaluated and found to be of the order of 15%. The 2D FFT was performed on the data in which the long wave structures were sized so as to ensure that the sampling lengths were much larger than the wavelengths of the spatial signals. The spatial resolution of the images was much better than the spatial frequencies of the shear instabilities.

IV. RESULTS AND DISCUSSION

A. Morphological Study

Four breakup regimes were observed over a wide range of operating conditions. They are first-wind induced, second-wind induced, bag breakup and fiber-type atomization regimes. Figure 4 shows example images of the flow cases and they illustrate these four typical breakup regimes. Note that these images were produced by applying background subtraction to the high-speed shadowgrams.

As mentioned in Sec. I, Hopfinger and Lasheras [5] and Dunand, Carreau, and Roger [14] observed hollow-cone sprays, which are caused by strong reversal air flows, when S goes beyond S_{cr}. Kumar and Sahu [17] observed hollow-cone sprays with high momentum ratios as well. However, in the present study, the hollow-cone spray structure does not appear in the flow cases where S goes beyond S_{cr} or where high M is achieved. This can be explained on the basis of the low kinetic energy that the central laminar liquid jet contains. The kinetic energy of the central laminar liquid jet in this present study is much smaller than the kinetic energy of the central turbulent liquid jets that Hopfinger and Lasheras [5], Dunand, Carreau, and Roger [14], and Kumar and Sahu [17] investigated. The hollow-cone spray structure indicates the interaction between the upward air flow motion towards the nozzle exit and the downward water jet motion. An equilibrium among the static pressure, the kinetic energy of the liquid jet and gas flow, and the ambient pressure should be achieved to sustain the hollow-cone spray structure[5]. However, in this present study, the kinetic energy inside the water jet is not high enough to fulfil the requirement, and as a result the upward air flows break the liquid jet directly into fibres instead (see Fig. 4d).

Figure 5 contains a regime map for the flow conditions listed in both Tables II and III, characterised by S and We_A. For high swirling flow cases with S ranging from 1.5 to 3.9, as the aerodynamic Weber number increases, the laminar liquid jet passes through the first-wind induced breakup regime, second-wind induced breakup regime, bag breakup regime and finally it falls within the fiber-type breakup regime. These four breakup regimes observed in this present study are consistent with what Lasheras and Hopfinger [7] found when they investigated a coaxial non-swirling jet. Note that for S in the range of $0.3 - 0.8$, the liquid jet falls within the boundary of the fiber type atomization when We_A increases to 1426. This indicates that with a further increase in We_A the fiber-type regime might control breakup of the liquid jet. As the swirl number increases from 1.2 to 2.5, the aerodynamic Weber numbers corresponding to the start of the bag and fiber-type breakup regimes reduce significantly (see Fig. 5). With a further increase in swirl number the boundaries do not change

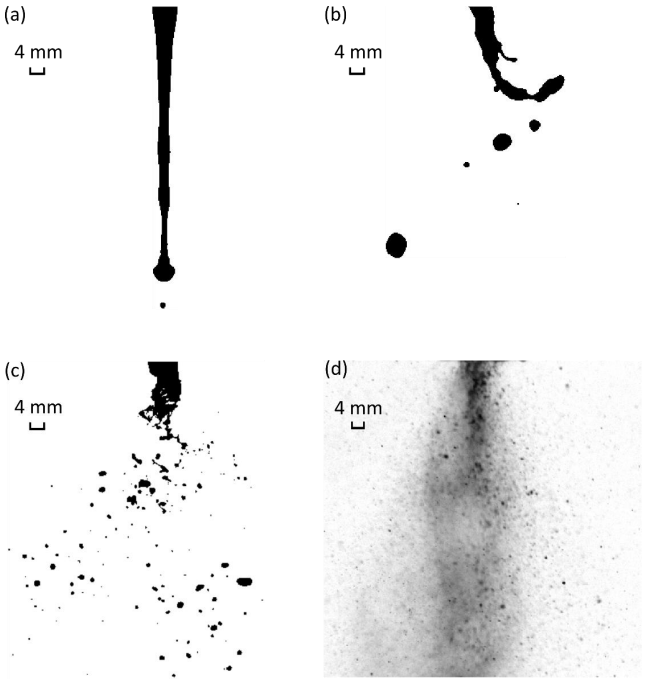

FIG. 4: (a) First-wind induced breakup regime ($S = 0$, $We_A = 9$). (b) Second-wind induced breakup regime ($S = 1.2$, $We_A = 40$). (c) Bag breakup regime ($S = 0.8$, $We_A = 158$). (d) Fiber-type atomization ($S = 2.5$, $We_A = 440$).

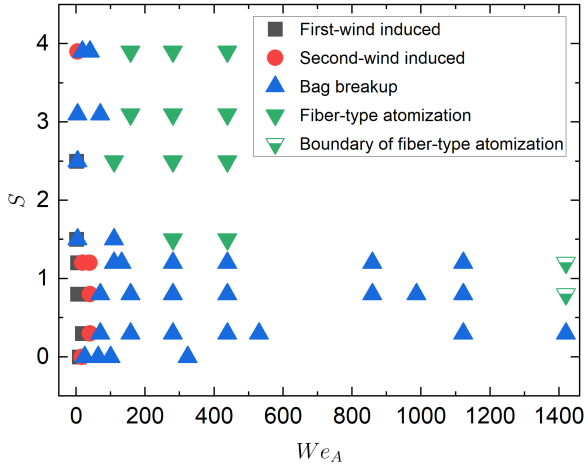

FIG. 5: Regime map characterised by S and We_A.

significantly. This indicates that air swirl promotes the morphological development of the jets, especially for the high swirling flow cases with S in the range of $1.2 - 2.5$. Note that for the non-swirling flow cases, the highest We_A that the atomizer can reach is 324, where bag breakup was observed. Lasheras and Hopfinger[7] found that further increases in We_A make the coaxial non-swirling jet enter the fiber-type breakup regime.

B. Breakup Length and First Droplet Location

The influence of aerodynamic forces, including the effect of air swirl on the breakup lengths and first droplet locations, is investigated here. Figures 6 and 7 show the relationships between the normalized breakup length (L/D_l) and the aerodynamic Weber numbers and swirl numbers. Figure 8 illustrates the relationships between the normalized first droplet location (Y/D_l) and the aerodynamic Weber numbers and swirl numbers. The first droplet location (Y) refers to the axial distance between the first droplet separation and the nozzle exit. Note that the central line of each box indicates the median. The top and bottom edges of each box represent 25^{th} and 75^{th} percentiles, respectively. Whiskers in the plot extend to the most extreme points. If sample values are more than 1.5 times the interquartile range away from the bottom or top edges of the boxes, they will be considered as "outliers" and will be plotted using plus symbols. For each box plot shown in figures 6, 7 and 8, the ratio of the number of "outliers" to the overall number of samples falls within the range of $\sim 0.4\% - 6.7\%$. When the aerodynamic Weber number increases, the medians of breakup lengths and the axial distances for the first droplet separation reduce. This can be explained on the basis of the increase in shear stress acting on the water-air interface, which leads to a more significant destabilization of the liquid jet. The addition of the swirling annular gas stream has a significant effect on reducing the breakup length of the liquid jet and axial distance for the first droplet separation, which indicates that the swirling annular air stream destabilizes the liquid jet more significantly compared with non-swirling annular air stream.

For the high swirling flow cases with S ranging from 1.2 to 3.9, one can observe from the high-speed shadowgraphy that after the droplets are generated, they are blown upwards to the positions near the nozzle exit and then are blown sideways by the annular swirling air jet. The upwards motions of the droplets are caused by the central reversal air flows, which is proven by SPIV and is discussed in Sec. IV C. Specially, for the high swirling flow cases with $S = 3.9$ and $We_A \leq 17$, the upwards motions of the droplets do not happen. This might be because less interaction between the water jet and the annular swirling air jet happens as S goes up, and the low We_A for these flow cases might result in the weak air flows. The central reversal air flows do not happen for the low swirling flow cases with S ranging from 0.3 to 0.8. Hence, the first droplet measurements are only performed for the flow cases with S ranging from 0 to 0.8.

Note that the optimum recording time duration and thresholding level were evaluated for each operating condition. The uncertainties of the non-dimensional breakup lengths and first droplet locations caused by the recording time duration and thresholding level were evaluated for each flow case and found to be small ($\sim$5%) (see Fig. 9 and Fig. 10). According to the Nyquist–Shannon sampling theorem, the minimum droplet size is specified as three pixels, which means that the droplets with sizes larger than 2 pixels are detected. The uncertainty of the first droplet locations caused by the smallest droplet size specified in the Matlab code is evaluated for each flow case

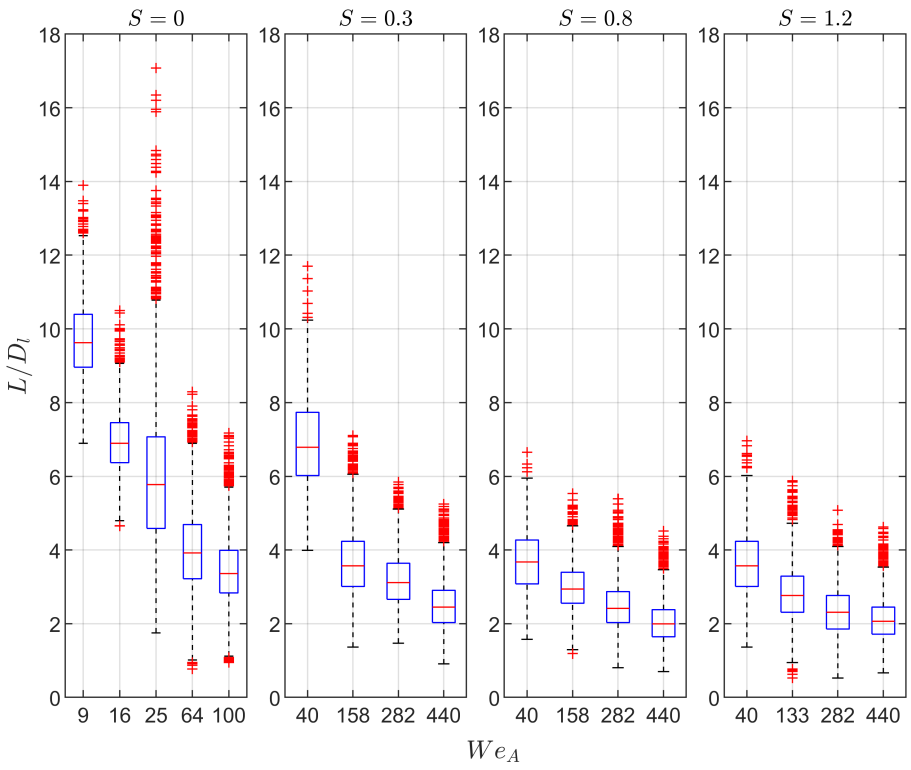

FIG. 6: L/D_l vs We_A for S in the range of $0 - 1.2$.

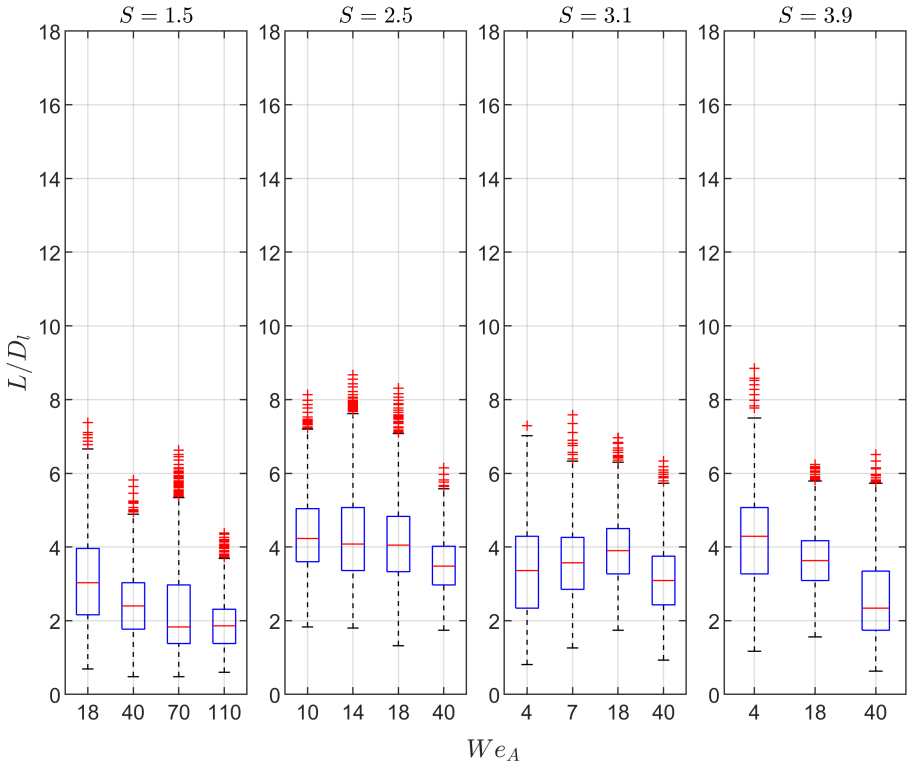

FIG. 7: L/D_l vs We_A for S in the range of $1.5 - 3.9$.

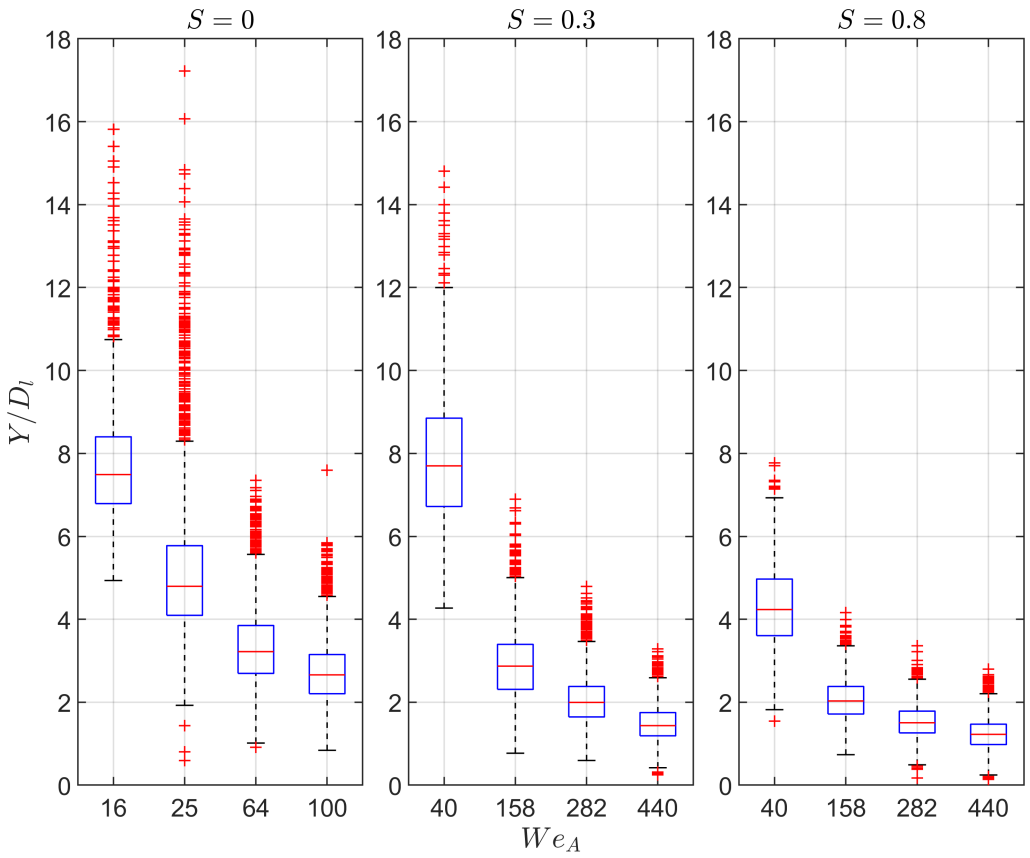

FIG. 8: Y/D_l vs We_A for various swirl numbers.

and found to be small ($\sim$6%) (see Fig. 11).

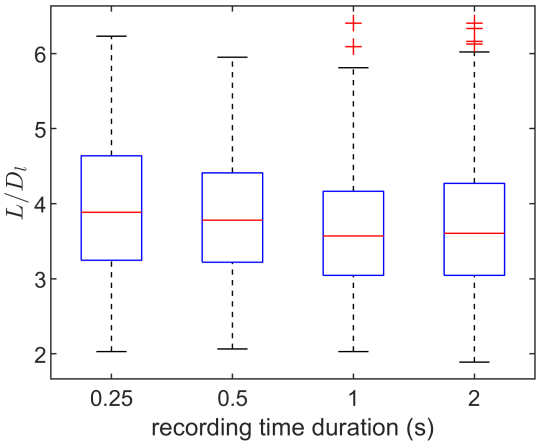

FIG. 9: L/D_l vs recording time duration for case 10.

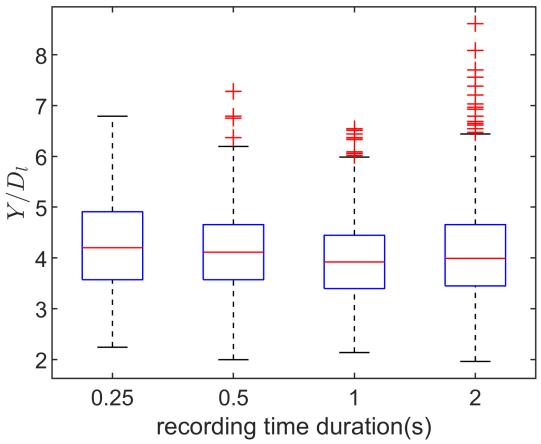

FIG. 10: Y/D_l vs recording time duration for case 10.

Eroglu, Chigier, and Farago [8] ejected a central water jet inside a non-swirling coaxial air jet with the liquid Reynolds numbers ranging from 1097 to 9328. With the same aerodynamic Weber number, the mean values of the breakup lengths for the water jet that they studied are longer than the ones detected in the present study. This is because their liquid Reynolds numbers are higher than the one in this paper. The Breakup length of a liquid jet in a coaxial gas jet is proportional to the axial velocity of the liquid jet at the nozzle exit[30].

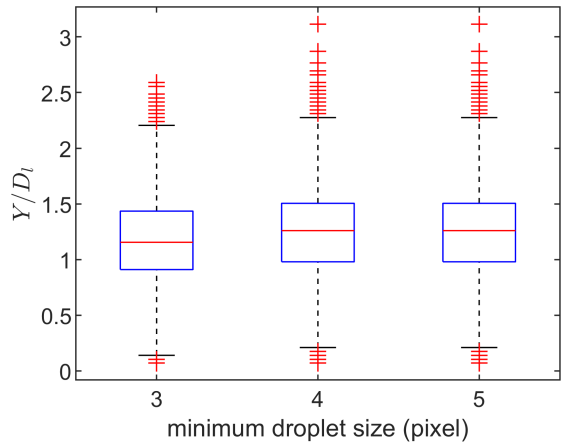

FIG. 11: Y/D_l vs minimum droplet size for case 13.

Kumar and Sahu [11] investigated the breakup length of a turbulent liquid jet in a co-annular non-swirling air jet with the momentum flux ratios ranging from 1 to 8. With the same momentum flux ratio the means of the breakup lengths that Kumar and Sahu [11] detected are much smaller than the ones measured in this paper. With the same momentum flux ratio, the aerodynamic Weber numbers in the literature are much larger than the ones used in the present work, which indicates that different breakup regimes might control breakup of the liquid jet with the same momentum flux ratio for Kumar and Sahu [11] and this study. Dumouchel [31] and Lasheras and Hopfinger [7] found that a complete regime map of a coaxial liquid-gas jet should be based at least on the momentum flux ratio, liquid Reynolds number and aerodynamic Weber number. Kumar and Sahu [12] measured the breakup length of a central turbulent water jet surrounded by a co-annular air flow with and without swirl over a wide range of aerodynamic Weber numbers $We_A(80-300)$, momentum ratios, $M(1-8)$, and swirl numbers, $S(0-0.8)$. They found that the breakup length decreases as We_A and S goes up, which is consistent with the results shown in this paper.

1. Breakup Length Model

We model the mean normalized breakup length, $\overline{L}/D_l$ rather than the individual L/D_l measurements. The mean of each of the randomized replicate measurements is used in the model. Randomized replicate measurements provide a measure of the effect of unobserved sources of variance as discussed by Montgomery [32] and by Gelman *et al.* [33]. The model proposed for $\overline{L}/D_l$ is expressed by:

$$\begin{aligned} \frac{\overline{L}}{D_l} &\sim \mathcal{N}(\mu_L, \sigma_L) \\ \mu_L &= b_0 We_A^{b_1} (b_2 S + 1)^{b_3} \\ \sigma_L &= \left(\mu_L^2\right)^{b_4} b_5 \end{aligned} \tag{12}$$

where $\mathcal{N}$ is the normal distribution, μ_L is the mean of the normal distribution, σ_L is the standard deviation of the distribution, S is the swirl number, We_A is the aerodynamic Weber number, and b_i, $i = 1,2,...,5$ are regression coefficients. As already discussed and shown in Fig. 6 and 7, the breakup length decreases as We_A and S increase, which the model in Eq. 12 allows for depending on the value of the regression parameter b_i in the model mean μ_L.

The power law form of μ_L and the We_A term are also present in the models presented by Eroglu, Chigier, and Farago [8] and Kumar and Sahu [11] for non swirling coaxial jets. Kumar and Sahu [12] present a model with a swirl term similar to the above but with the constant of 1 replaced with a regression parameter and with momentum flux ratio replacing the Weber number. None of the mentioned prior models made any assumption as to the stochastic distribution of the data, which here is assumed to be normally distributed.

The measured $\overline{L}/D_l$ and We_a for each value of S are plotted in Fig. 12. The data clearly suggest that the standard deviation is not constant. As the Weber number increases, the dispersion of the mean breakup length decreases. This is accounted for in the model standard deviation σ_L, which is proportional to the mean of the model μ_L. The standard deviation model allows either an increase or a decrease with μ_L depending on the regression parameter b_4 and is therefore not prejudiced in this respect. The model for σ_L and the associated priors are adopted from Gelman *et al.* [33].

Several models for the breakup length include the Reynolds number of the central water jet, Re_l, as a term, as presented by Eroglu, Chigier, and Farago [8] and Kumar and Sahu [11]. We agree that the breakup length also depends on Re_l in addition to We_A and S. Ideally μ_L in Eq. 12 should include a term with Re_l, possibly in the form $Re_l^{b_i}$. Since Re_l is constant at 480 for all the flow cases in the work presented here, adding any term that is a function of Re_l amounts to adding a second redundant constant term. In practical terms this would also make the regression problem ill-posed. For these reasons we are required to omit Re_l in the model for $\overline{L}/D_l$ given in Eq. 12.

In addition to the mentioned dimensionless numbers, the momentum flux ratio, M, has also been proposed as a parameter for L/D_l models by Leroux, Delabroy, and Lacas [9] and Kumar and Sahu [11]. In the present study, We_A and M are linearly correlated so the inclusion of a term in the form of M^{b_i} in μ_L in Eq. 12 becomes redundant. The linear correlation between We_A and M is the result of constant liquid surface tension and the liquid velocity being much smaller than the gas velocity.

Bayesian regression was performed for the the model Eq. 12 using the prior distributions given in Table IV. The Stan[34] probabilistic programming language for statistical inference, called through the RStan R package[35] was used. The No-U-turn sampler[36] (NUTS) algorithm was used for the Markov Chain Monte Carlo (MCMC) sampling of the posterior distributions of the model parameters. Four Markov chains with 15000 samples in each chain were drawn. The square term in the model for σ_L, along with b_4 and b_5 were limited to being strictly positive, to ensure a strictly positive σ_L as is required for the standard deviation of a normal distri-

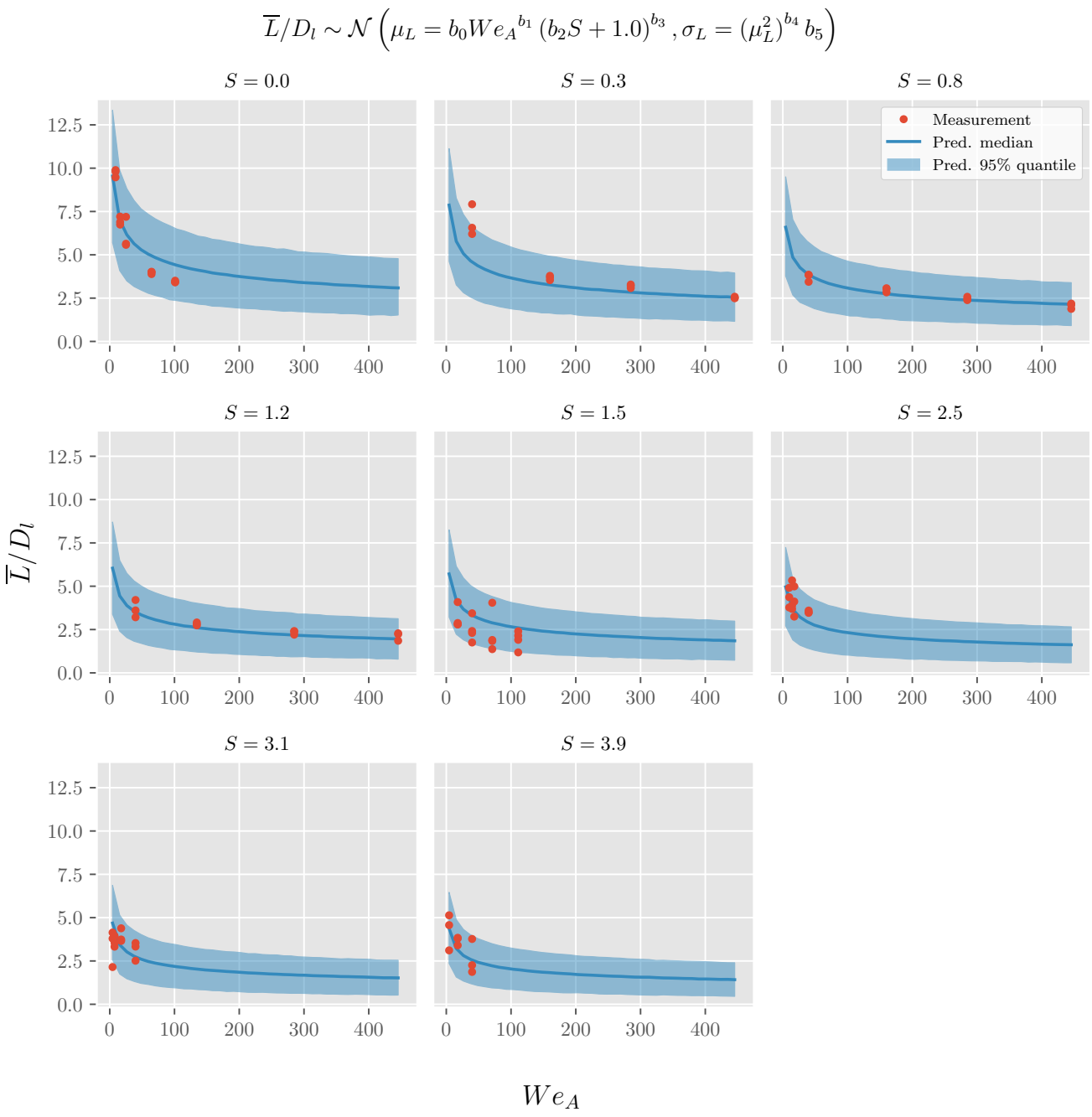

FIG. 12: $\overline{L}/D_l$ and We_A plot for various swirl numbers and model posterior predicted distributions for Eq. 12.

bution, which was chosen for the $\overline{L}/D_l$ model. The a_i parameters and associated prior distributions are used to model uncertainty in the values used for the b_i prior distributions. The posterior predicted distribution of $\overline{L}/D_l$ shown in figure 12 was obtained by random sampling of the model in Eq. 12 using the posterior parameter samples. Further details of this procedure are provided by Stan Development Team [34]. It should be noted that using the maximum a posteriori (MAP) parameter values provided in Fig. 13 and randomly sampling using the model Eq. 12 will in general lead to a narrower predicted distribution and is not a "fully Bayesian" approach to model prediction and validation since it omits the posterior distribution of the model parameter values, as discussed by Bishop [37].

Figure 12 shows that the posterior predicted distribution from the model of the normalized mean breakup length $\overline{L}/D_l$ is in good agreement with the measurements. The red dots show the measured values of $\overline{L}/D_l$ for various operating conditions, the blue lines show the median of the posterior predicted distribution of $\overline{L}/D_l$ and the shaded blue area represents the predicted 2.5% to 97.5% quantile interval (Pred. 95% in-

terval). The predicted median (Pred. median) is plotted instead of the mean because the median is less sensitive to outliers.

For $S = 0$ the model predicts slightly longer breakup lengths than observed as We_A increases. The largest discrepancy between model and observations occurs with $S = 0.3$ at small values of We_A where the model seems to predict a smaller breakup length than measured. As We_A increases the predicted median comes closer to the measurements and is in good agreement. The issue is not present for $S = 0.8$ and $S = 1.2$ where the predicted median is in good agreement with measurements for all values of We_A. For $0.0 \leq S \leq 1.2$ the posterior predicted 95% quantile interval seems to be too large given the relatively small dispersion in the measured breakup length.

As S increases above 1.2, the measurements cover more of the posterior predicted 95% quantile interval compared to smaller values of swirl. The predicted median still seems to be in good agreement with measurements apart from at $S = 1.5$ where the predicted median breakup length is larger. $S = 1.5$ seems to be somewhat of an outlier compared to both the smaller and larger swirl value cases, with a larger dispersion in measured values and may be indicative of a transition in breakup regimes.

Figure 13 shows the posterior parameter distributions. Kernel density estimation on the samples from all 4 chains was used to produce the posterior probability distribution shown with red lines. Further details on kernel density estimators are discussed by Bishop [37]. The effective sample size of (ESS) for each parameter is provided in Fig. 13. ESS is greater than 4900 for all parameters. $\hat{R}$ is a measure of convergence of multiple Markov chains as discussed by Vehtari *et al.* [38], Gelman *et al.* [33] and Kruschke [39]. For all parameter Markov chains $\hat{R} < 1.05$, which satisfies the rule of thumb for convergence provided by Kruschke [39].

None of the 95% highest probability density intervals for the parameters b_1, b_2, b_3 and b_4 include 0 which strongly suggests that, for the measurement data available, none of the terms in the assumed model in Eq. 12 are redundant. All of the terms in the model are needed to account for the distribution of the measured mean liquid core breakup lengths. This does not preclude the need for additional terms, as already discussed with respect to the liquid Reynolds number.

A swirl term of the kind proposed by Kumar and Sahu [12] (1.0 replaced with a regression coefficient) was also investigated using Bayesian regression but was found to have lower posterior model evidence[37] compared to the model in Eq. 12 by a factor of approximately $1/2$, with the log-marginal-likelihood of -147.1678 for the alternative swirl term compared to -146.5644 for the model in Eq. 12. The posterior model evidence was obtained using the bridgesampling[40] R package. Further details on bridge sampling are discussed by Gronau *et al.* [41].

Alternative model probability distributions were also investigated. The Student-T distribution, often used in Bayesian robust regression, and the exponentially modified Gaussian distribution, which allows skew distributions, were both investigated and found to have significantly smaller log-marginal likelihoods despite being having more degrees of freedom. The greater degrees of freedom in the two alternative distributions comes at the cost of a smaller log-marginal-likelihood when the measurements are accounted for by a simpler model as discussed by Bishop [37].

TABLE IV: Prior distributions used for the regression coefficients of the $\overline{L}/D_l$ model in Eq. 12.

Parameter	Interval[a]	Prior distribution
a_0	$(-\infty, \infty)$	$\mathcal{N}(\mu = 0, \sigma = 10)$
a_1	$[10^{-5}, \infty)$	Inverse gamma $(\alpha = 1, \beta = 1)$
b_0	$(-\infty, \infty)$	$\mathcal{N}(\mu = a_0, \sigma = a_1)$
b_1	$(-\infty, \infty)$	$\mathcal{N}(\mu = a_0, \sigma = a_1)$
b_2	$[0, \infty)$	$\mathcal{N}(\mu = a_0, \sigma = a_1)$
b_3	$(-\infty, \infty)$	$\mathcal{N}(\mu = a_0, \sigma = a_1)$
b_4	$[0, 1]$	Beta $(\alpha = a_1, \beta = a_1)$
b_5	$[10^{-5}, \infty)$	Inverse gamma $(\alpha = a_1, \beta = a_1)$

[a] The possible parameter values are not determined by the support of the prior distribution. They are instead limited to the given interval based on the data and the model. The prior is only used in determining the likelihood of the sampled value in the MCMC chain.

2. *First Droplet and Breakup Length Model*

As mentioned above, a central reversal air flow appears near the nozzle exit when $S \geq 1.2$, and some small droplets are blown upwards to the nozzle exit by these flow reversals. Hence, the first droplet measurements were only performed for the flow cases with S ranging from 0 to 0.8. The first droplet location (Y) refers to the axial distance between the first droplet separation and the nozzle exit.

The mean first droplet location $\overline{Y}/D_l$ and mean breakup length $\overline{L}/D_l$ for the three swirl values are plotted in Fig. 14. A linear correlation between $\overline{Y}/D_l$ and $\overline{L}/D_l$ is apparent. For small values of $\overline{L}/D_l$, the values of $\overline{Y}/D_l$ for all swirl values collapse to a line with small deviation. The variance increases somewhat with $\overline{L}/D_l$. For $S = 0.8$ there appears to be quadratic trend in $\overline{Y}/D_l$ as $\overline{L}/D_l$ increases. The same quadratic trend does not appear to be present for $S = 0$ and $S = 0.3$.

One would expect that, as the liquid core length decreases, the first droplets tend to appear closer to the nozzle (as apparent in Fig. 14). The creation of droplets requires the disintegration of a part of the liquid core. As the liquid core shortens, ligaments and by extension droplets must be created closer to the nozzle. However, it is does not immediately follow that there should be a linear relationship between the mean liquid core length and mean first droplet distance from the nozzle as seems to be the case based on Fig. 14.

As indicated by the $\overline{Y}/D_l = \overline{L}/D_l$ line in Fig. 14, as the liquid core length decreases, the first droplets tend to appear along the liquid core and upstream of the end of the liquid core based on the data points falling below the line. Conversely, as the liquid core length increases, the first droplets tend to cluster at the end of the liquid core. This is likely due to the

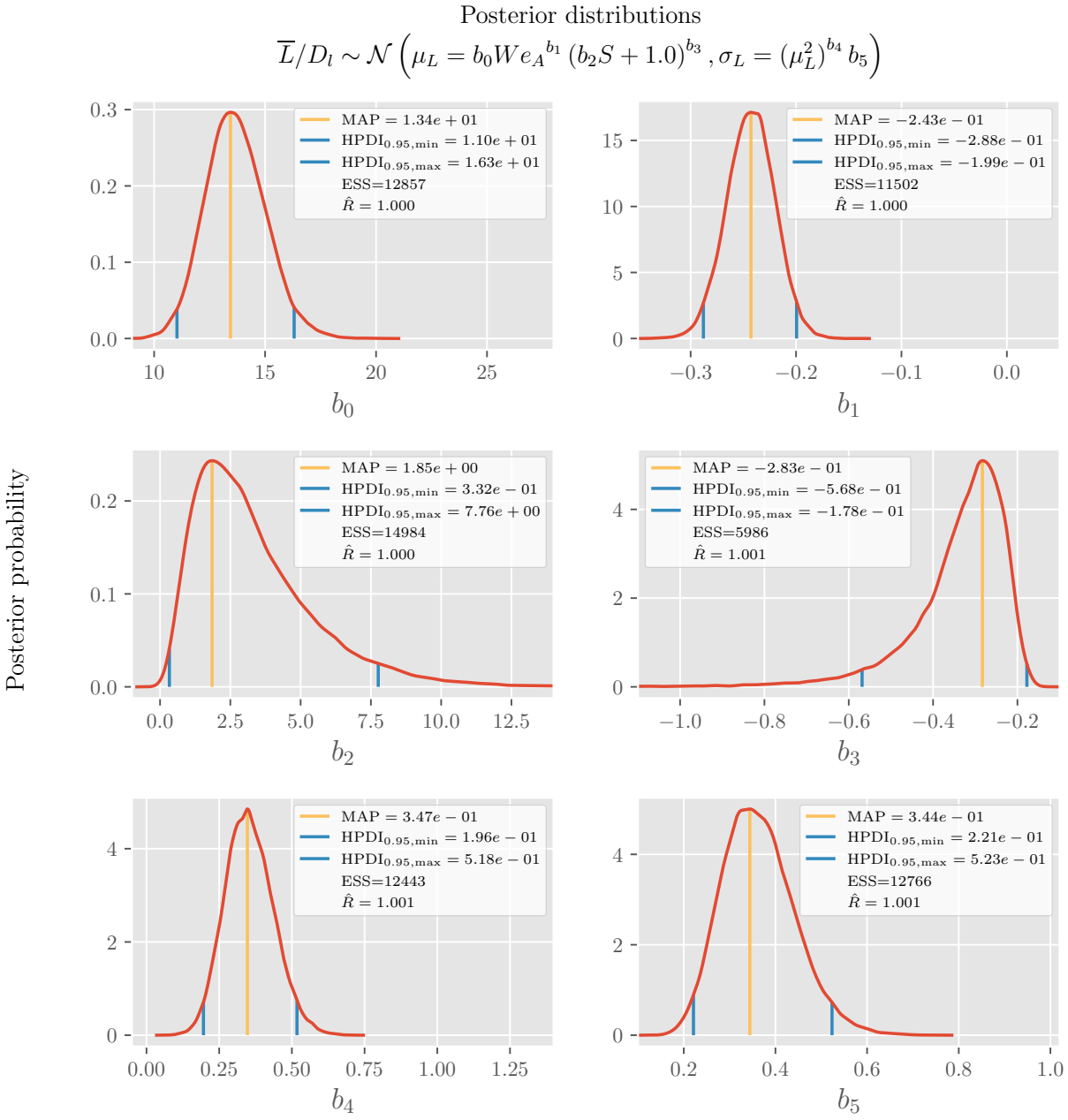

FIG. 13: Posterior distributions for parameters in Eq. 12. Probability distributions plotted with red lines are kernel density estimators on samples from all 4 Markov chains for each parameter. MAP, maximum a posteriori; $\text{HPDI}_{0.95,\text{min}}$, smallest boundary value of the 95% highest probability density interval; $\text{HPDI}_{0.95,\text{max}}$, largest boundary value of the 95% highest probability density interval; ESS, effective sample size; $\hat{R}$, MCMC chain convergence diagnostic.

change in breakup regime based on the illustration of breakup regimes in Fig. 4 and the breakup regime map in Fig. 5. As mean breakup length goes to 0, the mean first droplet location is expected to asymptotically approach a non zero value rather than go to 0. In the absence of a liquid core of any significance, the droplets will still have a mean location downstream of the nozzle. This is illustrated by the example shadowgram of fiber type breakup in Fig. 4.

Based on the preceding observations, the following model in Eq. 13 for the correlation between $\overline{Y}/D_l$ and $\overline{L}/D_l$ is proposed:

$$\frac{\overline{Y}}{D_l} \sim \mathcal{N}(\mu_Y, \sigma_Y)$$
$$\mu_Y = b_6 + b_7\left(\frac{\overline{L}}{D_l}\right) + b_8\left(\frac{\overline{L}}{D_l}\right)S + b_9\left(\frac{\overline{L}}{D_l}\right)^2 S \quad (13)$$

where, μ_Y is the mean of the normal distribution $\mathcal{N}$ for $\overline{Y}/D_l$ and σ_Y is the standard deviation. The terms in μ_Y involving S allow for the mean first droplet location to scale with swirl. The quadratic $\left(\overline{L}/D_l\right)^2$ term allows for the speculative quadratic trend in the data for $S = 0.8$ and non-zero asymptotic behaviour as the breakup length approaches zero in addition to a non-zero intercept term.

Bayesian regression was performed for the the model Eq. 13 using the prior distributions given in Table V. The Turing.jl package[42] in Julia[43] using the NUTS algorithm was used for the MCMC sampling of the posterior distributions of the model parameters. Four Markov chains with 15000 samples in each were drawn. The posterior distributions of the model parameters from the MCMC sampling are shown in Fig. 14. The probability distribution shown with a red line is kernel density estimator on samples from all 4 Markov chains as discussed previously. The measured mean first droplet locations $\overline{Y}/D_l$ agree well with the posterior predictive distribution as shown in Fig. 14. The posterior predicted distributions based on the model in Eq. 13 were obtained in the same way as discussed for the breakup length model in Eq. 12. The posterior predictive distribution for $\overline{Y}/D_l$ is determined from the posterior distribution of the parameters and the proposed model.

The model posterior predicted distribution is shown in Fig. 14 in terms of the predicted 2.5% to 97.5% interval (Pred. 95% interval) for all swirl values and the median (Pred. median) for each swirl value. The predicted medians for each swirl very nearly coincide at small breakup lengths with the discrepancy increasing with breakup length. This is in good agreement with the measured mean values. The mean first droplet location for $S = 0.8$ and the largest breakup length that were assumed to be indicative of a quadratic trend appear as outliers in the proposed model predictive distribution median. These measured values still fall within the model 95% quantile interval and so the model is not inconsistent with respect to the data. The predicted 95% interval has a very slight quadratic trend as the breakup length increases.

On inspection of the parameter distributions and the 95% highest probability density intervals, there is only support in the data and model for a linear model with the HPDI intervals for b_6 and b_7 not including 0. There is weak support for the influence of S on the mean droplet location given that the b_8 HPDI includes zero. Given the model and available data, the quadratic coefficient b_9 seems to firmly suggest no quadratic trend to the data since the HPDI is centered on 0 and the MAP value of b_9 is also close to 0.

The negative values of the HPDI and MAP for the intercept term b_6 reinforce that as the breakup length decreases, the mean first droplet location precedes the mean breakup length. However, the mean first droplet location would be upstream of the nozzle as the mean breakup length approaches 0 (which has been observed). This is not possible and suggests limits to the model.

Bayesian regression on each swirl case individually was also performed and suggested that a model like the one proposed in Eq. 13 for all the swirl cases was suitable given almost equal regression coefficient and standard deviation posterior distributions.

TABLE V: Prior distributions used for the regression coefficients of the $\overline{Y}/D_l$ model in Eq. 13.

Parameter	Interval	Prior distribution
a_0	$(-\infty, \infty)$	$\mathcal{N}(\mu = 0, \sigma = 10)$
a_1	$[10^{-5}, \infty)$	Inverse gamma $(\alpha = 1, \beta = 1)$
b_6	$(-\infty, \infty)$	$\mathcal{N}(\mu = a_0, \sigma = a_1)$
b_7	$(-\infty, \infty)$	$\mathcal{N}(\mu = a_0, \sigma = a_1)$
b_8	$(-\infty, \infty)$	$\mathcal{N}(\mu = a_0, \sigma = a_1)$
b_9	$(-\infty, \infty)$	$\mathcal{N}(\mu = a_0, \sigma = a_1)$
σ_Y	$[10^{-5}, \infty)$	Inverse gamma $(\alpha = a_1, \beta = a_1)$

C. Non-swirling and Swirling Air Flow Fields

The influence of air swirl on the air flow field is investigated here. During this SPIV campaign, the liquid jet was not flowing so that the air structures very near the outlet could be probed. The liquid injector was left in place. This section thus describes exclusively the air flow field introduced by the air passages. SPIV was performed on all the swirling cases except $S = 3.1$ and 3.9, where the seeding particles clogged the small passages of the air swirlers. The topologies of the air flow fields for S ranging from 0 to 2.5 are discussed first in this section. Note that we discuss flows with specific We_A in the following section, despite the fact that the liquid was not flowing. By this we mean to designate the air flows used to create a specific We_A. Since, when flowing, the liquid jet flow rate was not changed, it is the air flow rate that sets We_A.

Figure 15 shows selected projections of the 3D vector fields onto the 2D planes for different swirl numbers. The data in the images represent averages. Additional flow cases, together with the corresponding fluctuating components, are provided by Liang, Johansen and Linne[3]. Different colorbars are used in the subplots to emphasize the topology of the air flow field. The origin of the coordinate system is located at the center of the nozzle exit. For the non-swirling flow case, the annular air flows in the axial direction after leaving the nozzle, which leaves a central dark region with nearly zero velocity right below the water tube. The annular air flows for $We_A = 9$ start to converge at the downstream position of $1.5D_l$. As We_A goes up, the convergence of the annular air flow occurs slightly closer to the nozzle exit. The annular air flows start to converge $1.4D_l$ downstream when We_A increases to 100. For the swirling flow cases, the air flows start to expand radially after they leave the nozzle, as expected. The extent of the expansion becomes larger as S goes up, which would be expected to affect the evolution of the shear layers in the coaxial swirling air-water jets. When S remains constant, the extent of

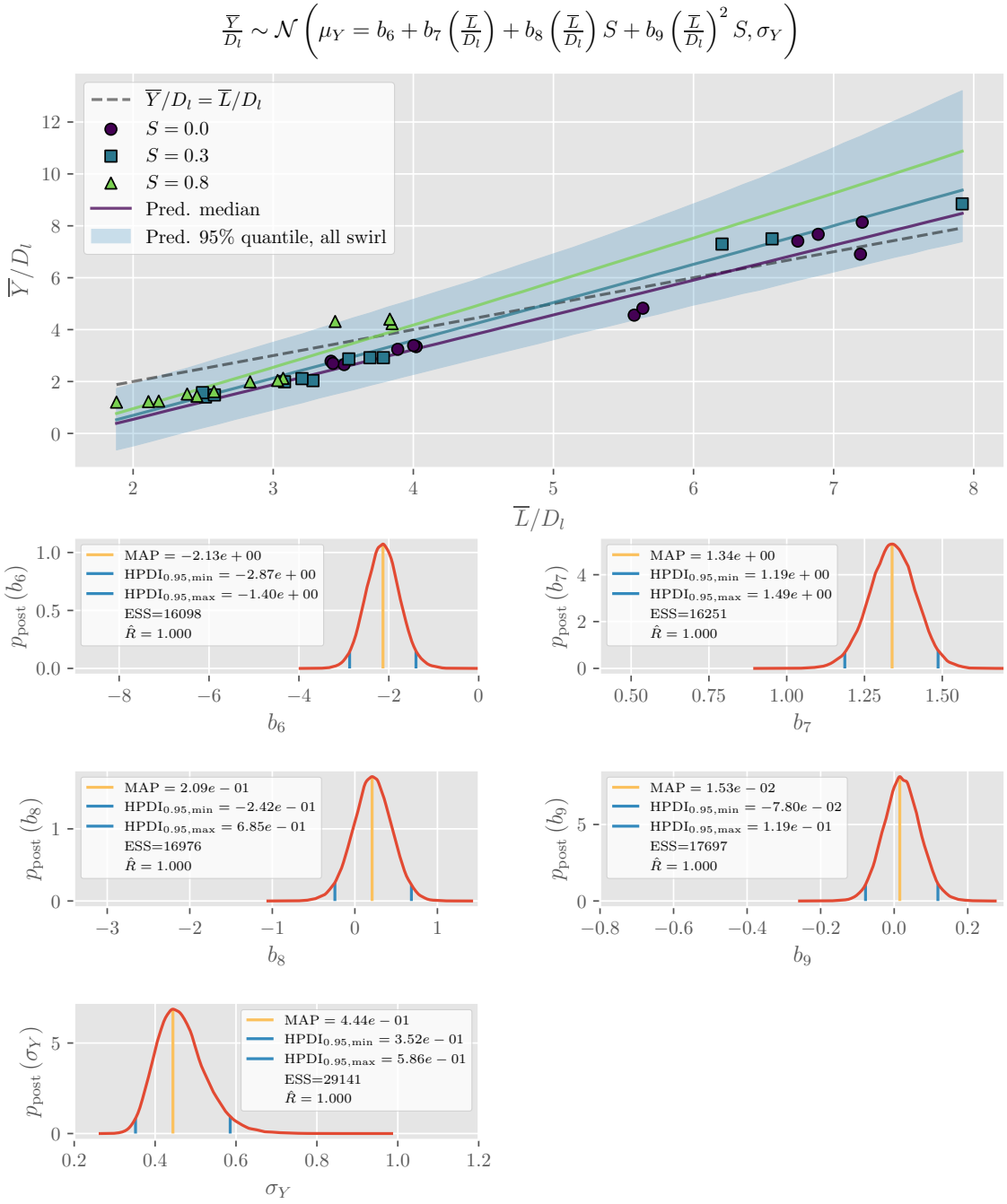

FIG. 14: $\overline{Y}/D_l$ and $\overline{L}/D_l$ correlation plot, $\overline{Y}/D_l$ model posterior prediction distribution and posterior distributions for parameters in Eq. 13. The predicted median (Pred. median) for each swirl value is shown with a solid line with the associated measurement plot colour. Probability distributions plotted with red lines are kernel density estimators on samples from all 4 Markov chains for each parameter. MAP, maximum a posteriori; $\text{HPDI}_{0.95,\min}$, smallest boundary value of the 95% highest probability density interval; $\text{HPDI}_{0.95,\max}$, largest boundary value of the 95% highest probability density interval; ESS, effective sample size; $\hat{R}$, MCMC chain convergence diagnostic.

the radial expansion of the annular swirling air flows does not change when We_A varies, which indicates that S determines the extent of the expansion. Note that the velocity maxima in the subplots for the swirling flow cases are different and lower than the non-swirling flow case. This occurs because the flow cross sectional area expands right at the exit, and the expansion increases with S.

The velocity data collected at the downstream positions of $0.27D_l$ and $0.43D_l$ were substituted into Eq. 4, respectively, to calculate the measured swirl number. It was found that the swirl numbers calculated from those two data sets were consistent with each other. The differences between the measured and geometrical swirl numbers range from 48% to 66% (see Table I in Sec. II B). The air swirl strength dissipated somewhat after very little displacement downstream, i.e. where the measurement was taken. The ideal case would be to collect the velocity data at the nozzle exit to calculate the measured swirl number. However, since the flow was highly three-dimensional and the air passages of the air swirlers were narrow compared with the cross-sectional area of the co-flow tube, low graphite particle density was observed at the nozzle exit, which made it difficult to measure the air flow fields at the nozzle exit. It is also true that Eq. 5 is a fairly simplified design guideline. Note that in this work, the geometrical swirl numbers (S) were used to describe the operating conditions of the atomizer. For simplicity, the term "swirl number" mentioned throughout the sections of this work refers to the "geometrical swirl number".

Figure 16 shows the relationship between the magnitude of the 3-D velocity and the radial position (X). Note that the data are collected at the axial position of $0.6D_l$ downstream. For each velocity profile, there are two peaks, one at each side of the central axis of the nozzle, and these peaks start to move outward significantly when S goes above 0.8. When S increases from 0.8 to 2.5, the locations of the peaks move from $X = 4.6$ mm (or -3.3 mm) to $X = 8.6$ mm (or -8.6 mm). This can be explained by the fact that the annular air flows expand further in the radial direction when S increases. The velocity profiles reach a local minimum (< 4 m/s) on the central axis of the nozzle ($X = 0$ mm). The magnitude of the velocity decreases to zero on the boundary between the annular air flow and the ambient, stagnant air.

Figure 17 shows the relationship between the axial velocity and the radial position. The reversal flows start to appear near the central axis when S increases to 1.2. This can explain why the droplets that are located near the nozzle exit move upwards in the high-speed shadowgrams of the high swirling flow cases ($S \geq 1.2$). A further increase in S results in significant expansion of the central reversal air flow region.

Figure 18 contains the radial profiles of the velocities in the out-of-plane direction (W) at the axial position of $0.6D_l$ downstream. For each velocity profile, W reaches its maximum and minimum at the right and left sides of the central axis of the nozzle, respectively. The radial locations that W reaches its maximum and minimum move outward when S goes up. They grow from $X = 4$ mm (or $X = -3.3$ mm) to $X = 8.6$ mm (or $X = -8.6$ mm) when S increases from 0.3 to 2.5. This means that the region where the significant out-of-plane motion of the swirling air can be observed expand further when S goes up. This is consistent with the development of the two-dimensional topologies of the air flow fields as S varies, which is mentioned above.

Figure 19 shows the evolution of the inner and outer shear layers for various swirl numbers, based on vorticity maps. Note that a shear layer is defined as the layer where the velocity gradient starts. One can see that there are two inner shear layers (ISL) and two outer shear layers (OSL) in each subplot. For simplicity, one ISL and one OSL are marked in each subplot because the vorticity maps are symmetric. An increase in S results in a shift of the marked shear layers towards the upper-left corner of the image. That is caused by the fact that an increase in S leads to further expansion of the annular swirling air flows, as mentioned above. When S remains constant, the locations of the shear layers do not change significantly as We_A is varied. This can be explained by the fact that S determines the extent of expansion of the annular swirling air flows, as mentioned above.

D. Spatial and Temporal Features of Large-scale Instabilities

The effect of aerodynamic forces and the strength of the air swirl on spatial and temporal features of the large-scale instabilities is investigated here. POD was performed on the high-speed shadowgrams for all the flow cases, to find the dominant large-scale instability modes of the liquid jets. Figure 20 shows the topologies of the different types of the large-scale instabilities depicted by various POD modes for the flow cases with different swirl numbers and the same We_A. For each subplot, the values are normalized by their respective maxima. As shown in Figure 20, the dominant breakup modes for all the flow cases are flapping modes, which are depicted by the first POD mode. This mode is characterised by the flapping tail end of the liquid jet, as illustrated in Fig. 21. The wavy breakup modes, which are characterised by the bending/twisting of the liquid jet before it experiences breakup, appear as the secondary breakup mode for $S = 0.3$ and $S = 0.8$. The explosive breakup modes, which are characterised by the hollow-cone spray structure, appear as the secondary breakup mode for $S = 0$ and $S = 1.2$.

Generally, the singular value distribution of a principal component is used to evaluate how important that principal component is among all the principal components. The singular value distribution (ε_i) of a principal component is given by:

$$\varepsilon_i = \frac{\lambda_i}{\sum_{j=1}^{j=r} \lambda_j}, i \geq 1, \tag{14}$$

where λ_i is the singular value for that principal component, and r is total number of non-zero singular values and the rank of $\boldsymbol{K}$ in Eq. 9. Figure 22 shows the singular value distributions for the flapping modes as a function of We_A (or, alternatively, M). Note that all the flapping modes in Figure 22 are depicted by the first POD mode, and $\varepsilon_{\text{flap}}$ is the median of the multiple samplings for each flow case. It can be seen that $\varepsilon_{\text{flap}}$

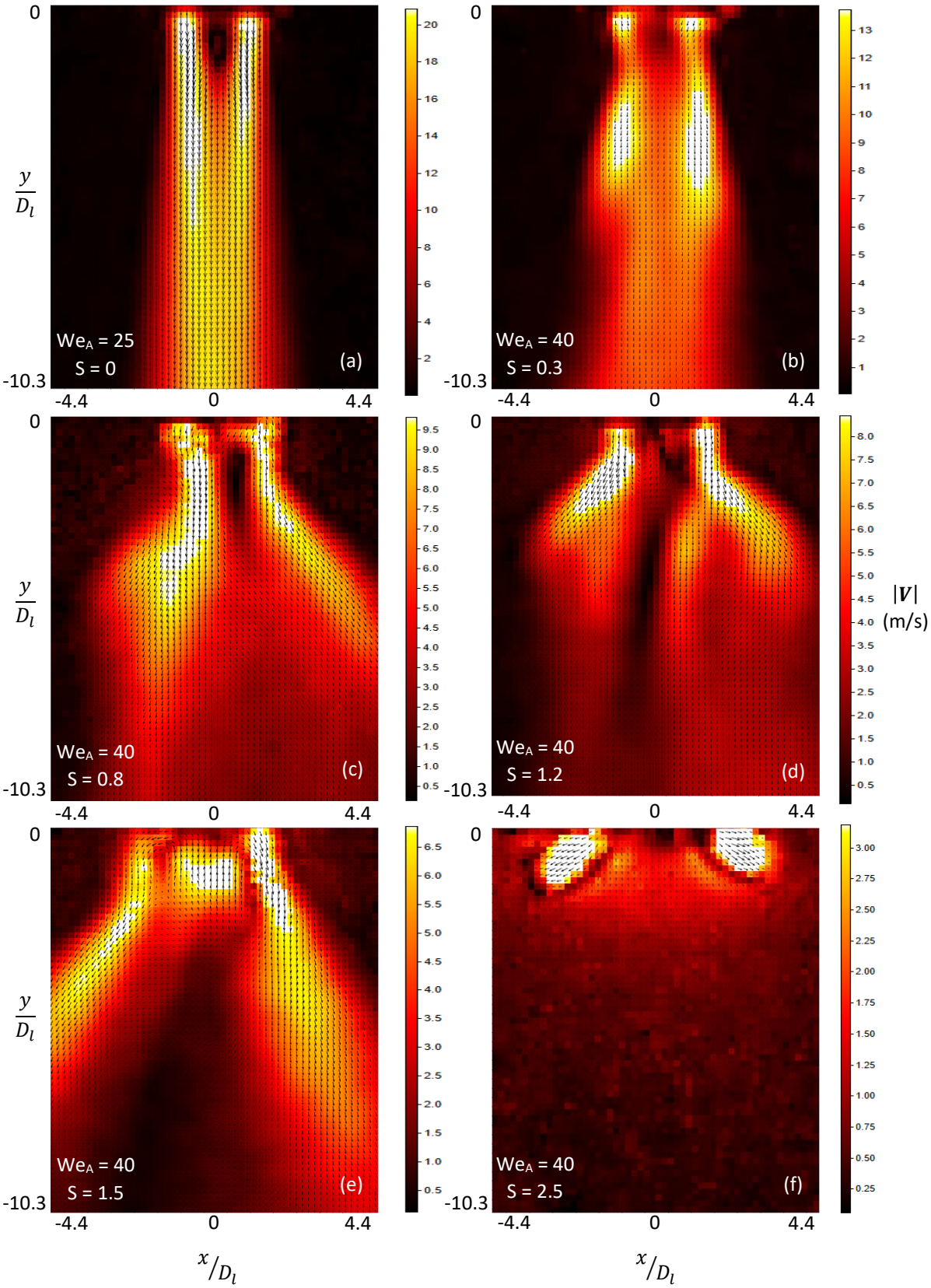

FIG. 15: 3D vector fields projected onto the 2D planes for various swirl numbers.

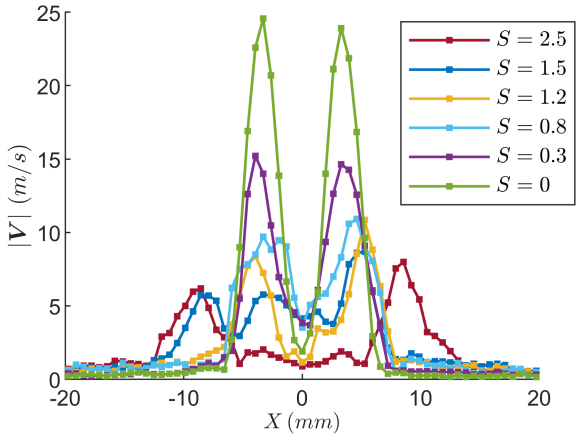

FIG. 16: $|\boldsymbol{V}|$ vs X for various swirl numbers at $y = 0.6D_l$. $We_A = 40$ for $S \neq 0$; $We_A = 25$ for $S = 0$.

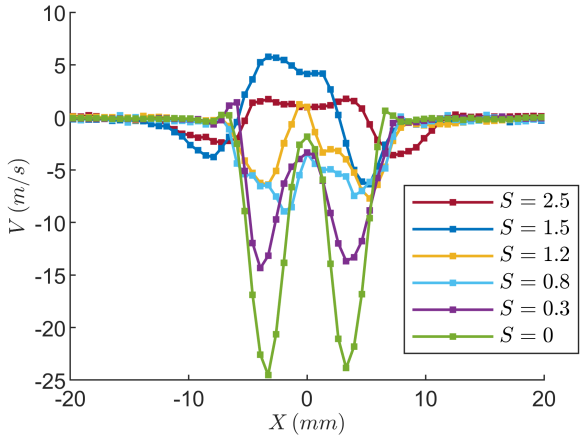

FIG. 17: V vs X for various swirl numbers at $y = 0.6D_l$. $We_A = 40$ for $S \neq 0$; $We_A = 25$ for $S = 0$.

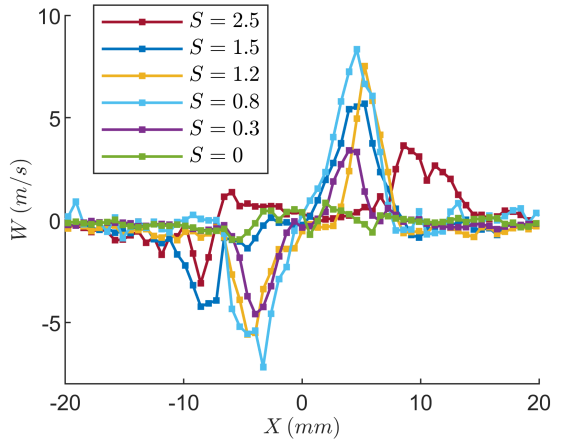

FIG. 18: W vs X for various swirl numbers at $y = 0.6D_l$. $We_A = 40$ for $S \neq 0$; $We_A = 25$ for $S = 0$.

decreases as We_A grows, which implies that further increases in We_A may change the topology of the first POD mode.

Figures 23 and 24 illustrate the large-scale instability regime maps characterised by the swirl number and aerodynamic Weber number (or, alternatively, M). Note that We_A and M are linearly correlated in the present study, as mentioned in Sec. IV B 1. For each flow case, a data point for a certain operating condition is considered on the boundary if only one sampling of the POD data shows clear instability. If there is no evidence for clear instability, it will be assumed to have no clear mode. If there are more than one sampling with evidence for instability, the instability will be plotted. Figure 23 indicates that the flapping instabilities dominate across all the flow cases. Apart from the flapping instability, Kumar and Sahu [17] observed an explosive breakup mode when they investigated the breakup of a central turbulent water jet by a co-annular air jet with and without swirl. They found that the dominant breakup mode changes from the flapping mode to the explosive breakup mode when the momentum ratio is high ($\sim$26). In the present study, however, for some flow cases with momentum ratios in the range of $\sim 15-660$, the explosive breakup modes appear as a secondary breakup mode rather than a dominant breakup mode (see Fig. 24). This can be explained on the basis of the low kinetic energy that the central laminar liquid jet contains, as discussed in Sec. IV A. Kumar and Sahu [17] also observed the wavy breakup mode, and they found that wavy breakup mode appears as the secondary breakup mode when the momentum ratio falls within the range of $\sim 1-5$. They also found that further increases in M make the secondary breakup mode change from wavy breakup mode to explosive breakup mode, and the explosive breakup mode subsequently changes to flapping mode when the momentum ratio is high ($\sim$26). Figure 24 illustrates that the wavy, explosive and flapping breakup modes appear as the secondary breakup mode over a wide range of operating conditions in this study. The wavy and explosive breakup modes happen when We_A is low (≤ 110). The flapping breakup modes appear for $S = 0.8$ with high We_A in the range of $\sim 282-440$, and for $S = 0$ with We_A of the order of 324.

How the aerodynamic forces and the strength of the air swirl influence the frequency of the flapping instability is investigated next. Performing a fast Fourier transform (FFT) on the first column of the matrix $\boldsymbol{V}$ obtained from SVD yields the frequency of the first POD mode (Eq. 9). Figure 25 illustrates the relationships between the frequencies of the flapping instabilities and aerodynamic Weber numbers/swirl numbers. Note that each data point in Figure 25 represents the flapping instability, which is depicted by the first principal component. For the non-swirling and low swirling flow cases ($0 \leq S \leq 0.8$), the frequency of the flapping instability increases as We_A grows, which indicates that the growth of the aerodynamic forces destabilizes the liquid jet more significantly without the presence of the central reversal air flows. For flow cases with S in the range of $\sim 0.3-0.8$, an increase in S results in the growth of f_{flap}, which indicates that the growth of the strength of the air swirl enhances the flapping instability when there are no central reversal air flows. This effect is stronger especially

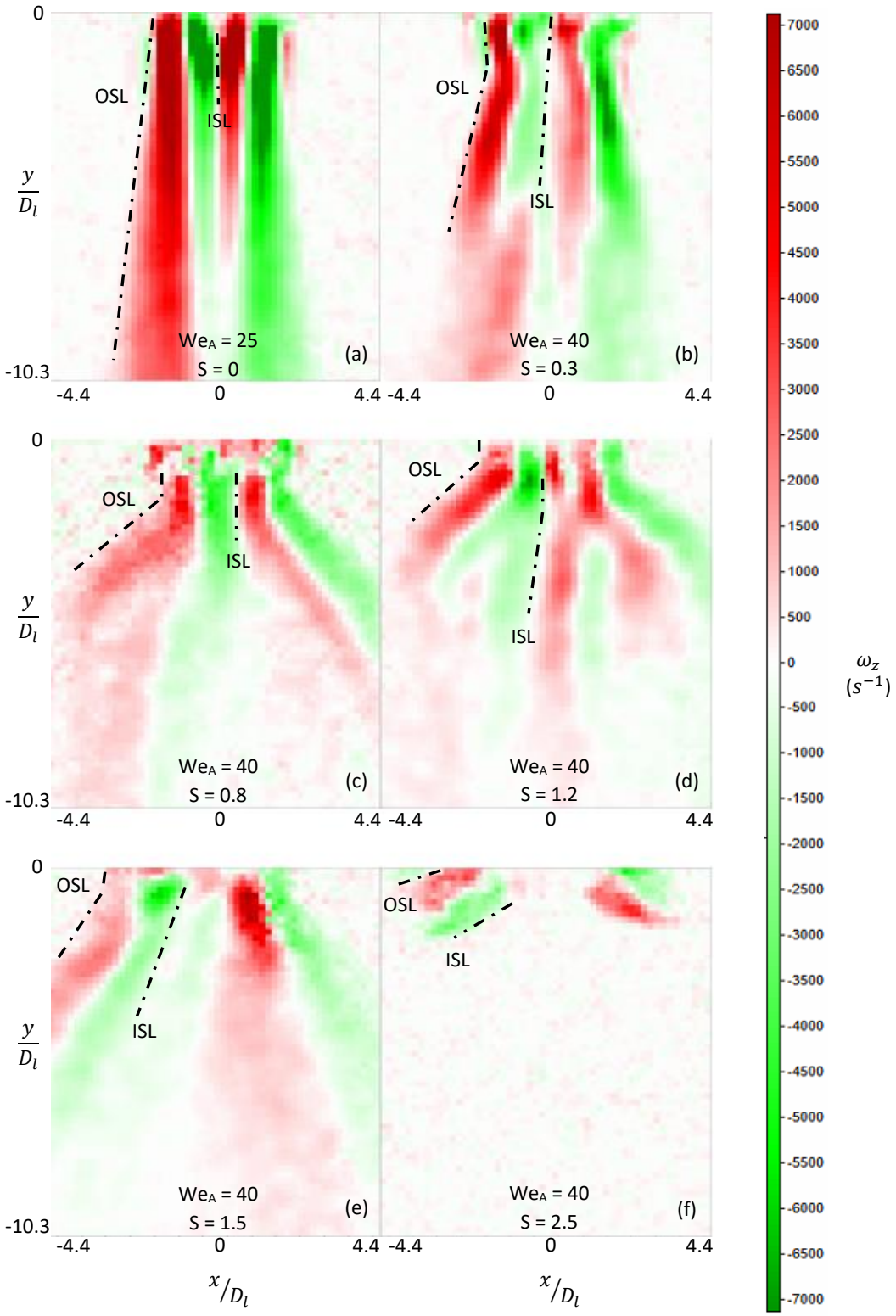

FIG. 19: Vorticity maps for various swirl numbers. OSL: outer shear layer; ISL: inner shear layer.

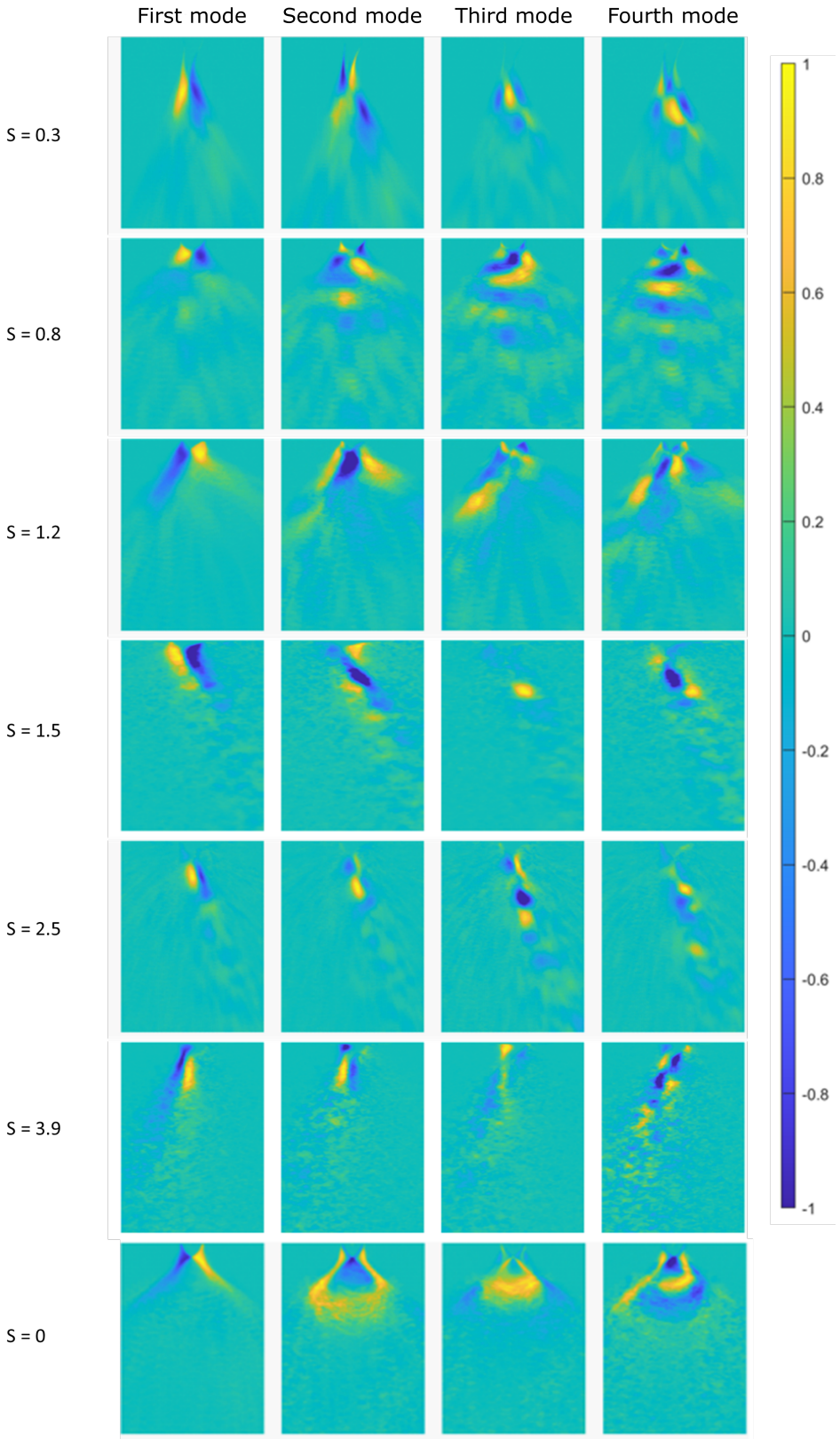

FIG. 20: First four POD modes for swirling flow cases with different swirl numbers and $We_A = 40$, and for non-swirling flow case with $We_A = 25$.

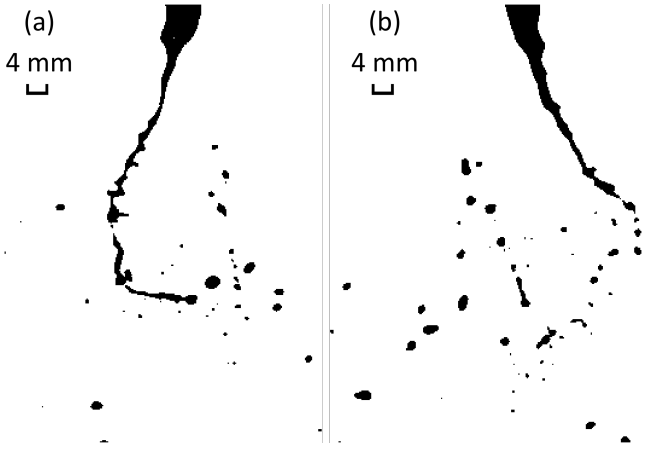

FIG. 21: Images of the flapping instability ($S = 0$, $We_A = 25$). Note that (a) and (b) represent two extreme spatial positions of the liquid jet within one period of the flapping instability.

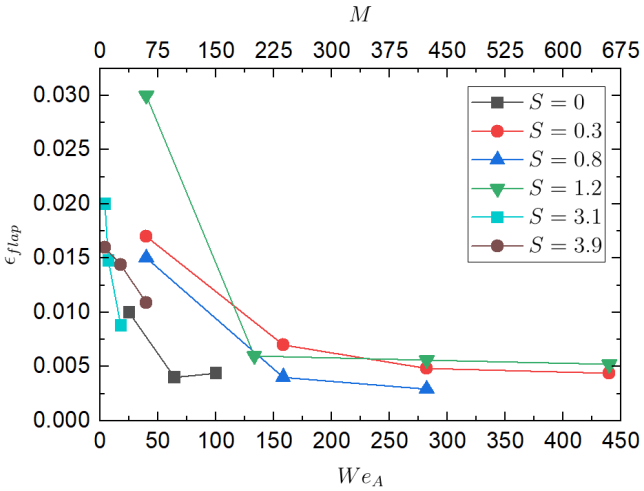

FIG. 22: Singular value distributions for the flapping modes depicted by the first principal component.

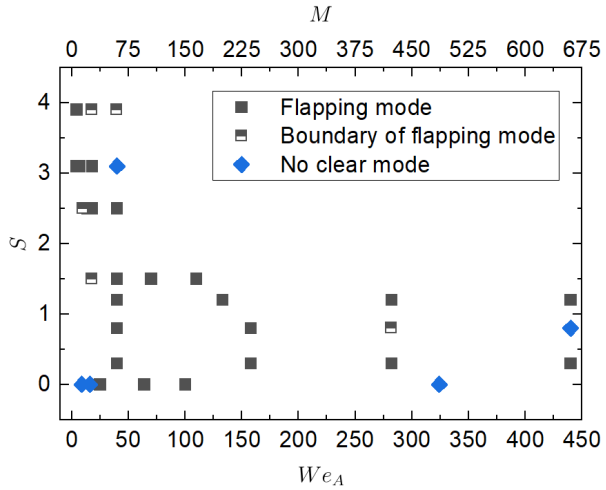

FIG. 23: Dominant breakup mode depicted by the first principal component.

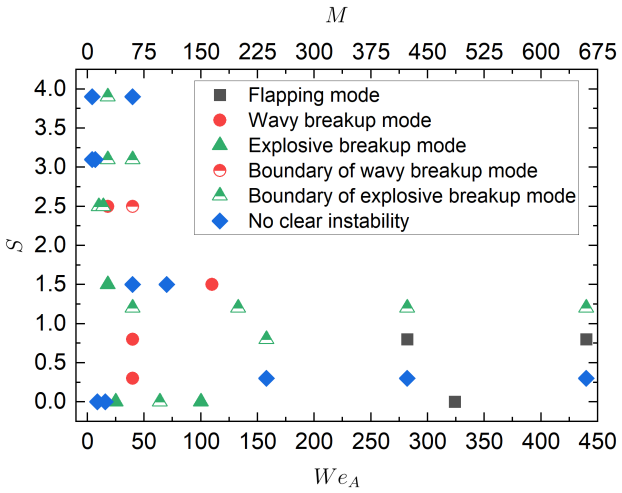

FIG. 24: Secondary breakup modes depicted by the second principal component.

for the flow cases with medium aerodynamic Weber numbers ($158 \leq We_A \leq 282$). Note that the data for the high swirling flow cases ($1.5 \leq S \leq 3.9$) are included in the grey zone. As mentioned in Sec. IV C, the central reversal flows happen when S falls within the range of $\sim 1.2 - 3.9$. For the high swirling flow cases with We_A's in the range of $\sim 4 - 133$, f_{flap} remains steadily below 37 Hz. The frequencies of the flapping instabilities for the high swirling flow cases are smaller than those for the low swirling flow cases, which indicates that the central reversal flows inhibit the flapping instability. For the high swirling flow cases, an increase in S reduces the frequency of the flapping instability. The reason behind this is that for the high swirling flow cases, after the annular swirling air flows leave the nozzle exit, the extent of the radial expansion is larger than for the low swirling flow cases. An increase of S causes further radial expansion of the annular swirling air flows, leading to weaker interaction between the central water jet and the annular swirling air jet, inhibiting the flapping instability.

E. Spatial and Temporal Frequencies of Shear Instabilities

In order to investigate how the aerodynamic forces and air swirl influence the shear instabilities on the air-water interfaces, the left-hand-side air-water interface positions were captured at many different moments in time, and a two-dimensional FFT was performed on the data to obtain the temporal (f_t) and spatial (f_x) frequencies of the shear instabilities. These temporal and spatial frequencies were detected in the cases 3, 6, 10, 14 and 30 (see Fig. 26 and Fig. 27). This was as expected because the long wave structures were observed in the high-speed shadowgrams for these five flow cases. There are no clear temporal and spatial frequencies for

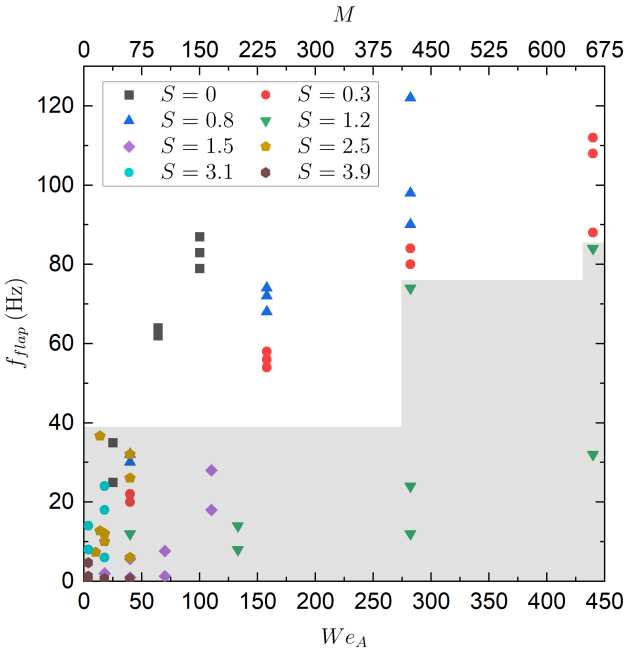

FIG. 25: f_{flap} vs We_A for various swirl numbers. The data for the high swirling flow cases ($1.5 \leq S \leq 3.9$) are included in the grey zone.

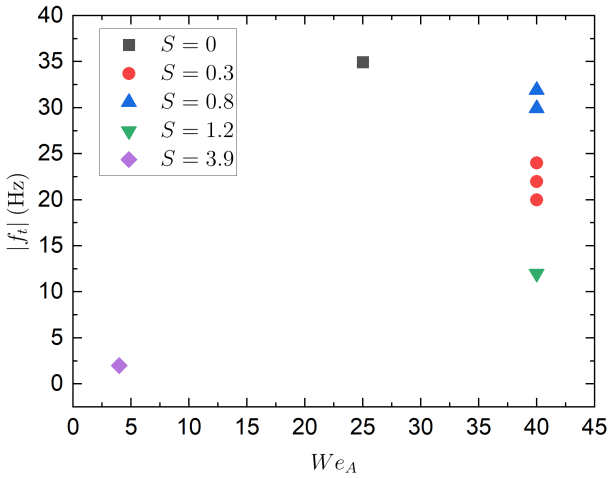

FIG. 26: Temporal frequency $|f_t|$ vs We_A for the cases 3, 6, 10, 14 and 30.

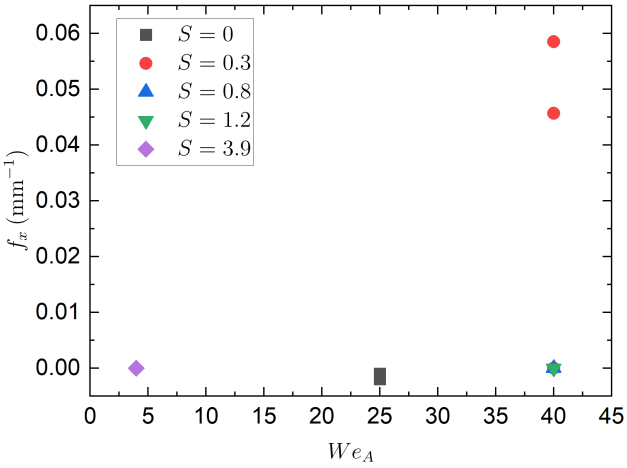

FIG. 27: Spatial frequency f_x vs We_A for the cases 3, 6, 10, 14 and 30.

the rest of the flow cases. For the non-swirling flow cases with $We_A \leq 16$, long wave structures are observed, but there are no clear temporal and spatial frequencies for these flow cases. This can be explained by the fact that the wave structures in the high-speed shadowgrams for those non-swirling flow cases have much lower amplitude than the wave structures observed in the cases 3, 6, 10, 14 and 30. However, for the case 3 ($S = 0$ and $We_A = 25$), the flapping instability starts to appear, which increases the amplitudes of the long wave structures to some extent (see Fig. 23). This might account for the temporal and spatial frequencies that were observed in the case 3. Further increases in We_A with $S = 0$ decrease the breakup lengths, which shortens the wave structures. This results in the absence of clear temporal and spatial frequencies for the cases 4 and 5. For the low swirling flow cases ($0 < S \leq 0.8$), $|f_t|$ increases as S goes up, which indicates that an increase in the strength of the air swirl increases the temporal frequency of the shear instability. However, the temporal frequency of the instability reduces significantly when S increases to 1.2. The reason behind this is that the reversal flows starts to appear when $S \geq 1.2$, as mentioned in Sec. IV C, and the reversal flows tend to stabilize the air-water interfaces. A further increase in S from 1.2 to 3.9 makes $|f_t|$ drop to 2 Hz. The spatial frequencies remain low (≤ 0.06 mm^{-1}) for the cases 3, 6, 10, 14 and 30.

V. CONCLUSIONS

The goal of the present work is to develop a comprehensive database for spray formation caused by shear forces, in part by removing turbulence from the liquid jet. In addition to turbulence, cavitation, and shear forces, capillary forces will also contribute (e.g. during liquid column pinch-off) just as they do during Rayleigh breakup. In order to investigate how the strength of the air swirl influences the spray formation, air swirl is introduced into the annular air flows using four-vane swirlers with S in the range of $0.3 - 3.9$. High-speed shadowgraphic visualization was performed over a wide range of breakup regimes. Data post-processing was applied to the high-speed shadowgrams to measure the breakup lengths and first droplet locations. Scaling of the normalized breakup lengths and first droplet locations is proposed in this work.

2D FFT and POD were performed on the high-speed shadowgrams to obtain 2D spectra and detect the large-scale instabilities, respectively. In order to investigate how the strength of the air swirl influences the air flow field, SPIV measurements were performed on the annular air jets with S in the range of $0-2.5$. The following statements are concluded from the measurements.

1. Four breakup regimes were observed over a wide range of operating conditions. They are first-wind induced, second-wind induced, bag breakup and fiber-type atomization regimes. Air swirl promotes the morphological development of the jets, especially for the high swirling flow cases with $1.2 \leq S \leq 2.5$.

2. Both the normalized breakup length and first droplet location are normally distributed. A quadratic relationship between the medians of the normalized breakup lengths and first droplet locations was found.

3. Radial expansion of the annular swirling air jets was observed near the nozzle exit. The extent of the radial expansion of the swirling air flows becomes larger as S goes up. Consequently, an increase in S leads to the shift of the shear layers towards the positions which are right below the outer edges of the co-flow tube. A central reversal air flow was observed when $S \geq 1.2$.

4. POD was performed on the high-speed shadowgrams for all the flow cases to find the dominant large-scale instability modes of the liquid jets. It was found that flapping instabilities dominate across most of the flow cases, as revealed by the first POD mode. Wavy and explosive breakup appear as the secondary breakup modes when We_A is low (≤ 110). In the absence of the reversal air flows, an increase in the aerodynamic forces destabilizes the liquid jet more significantly. For the low swirling flow cases ($0 < S \leq 0.8$), increasing the strength of the air swirl enhances flapping instabilities. The reversal flow inhibits the flapping instability, and an increase in S reduces the frequency of the flapping instability when $S \geq 1.2$.

5. Air-water interface positions were captured at many different moments in time, and a two-dimensional FFT was performed on the data to obtain the temporal and spatial frequencies of the shear instabilities. The temporal and spatial frequencies of the shear instabilities were detected in the flow cases which have long wave structures. In the absence of the central reversal air flows, increasing the strength of the air swirl increases the temporal frequency of the shear instability. A significant reduction of the temporal frequency of the shear instability was observed when $S \geq 1.2$, which implies that the central reversal air flows tend to stabilize the air-water interfaces. The spatial frequencies remain low ($\leq 0.06\ \mathrm{mm}^{-1}$) across all the flow cases which show the long wave structures.

6. Few droplets were observed in the high-speed shadowgrams over the operating conditions shown in Table II (the high speed videos for those flow cases can be found in the database[3]). Those drop sizes are big when compared with the drops produced by the flows defined in Table III. Many smaller droplets were produced when the liquid jet entered the fiber-type breakup regime. The drop size measurements for those flow cases, determined using a phase Doppler particle size analyzer, will be presented in a forthcoming publication[24].

ACKNOWLEDGMENTS

This work was supported in part by EPSRC grants number EP/P020593/1 and EP/P011438/1. Several plots were generated using the Matplotlib Python library[44].

DATA AVAILABILITY STATEMENT

The data that support the findings of this study are openly available in Edinburgh DataShare at https://doi.org/10.7488/ds/3459.

REFERENCES

[1] A. H. Lefebvre and V. McDonell, *Atomization and Sprays (2nd Edition)* (CRC Press, 2017).
[2] J. B. Heywood, *Internal Combustion Engine Fundamentals* (McGraw-Hill, 2018).
[3] Y. Liang, L. C. Johansen, and M. Linne, "Breakup of a laminar liquid jet by coaxial non-swirling and swirling air streams," University of Edinburgh (2022), dataset. https://doi.org/10.7488/ds/3459.
[4] R. D. Reitz and F. Bracco, "Mechanisms of breakup of round liquid jets," The Encyclopedia of Fluid Mechanics **3**, 223–249 (1986).
[5] E. J. Hopfinger and J. C. Lasheras, "Explosive breakup of a liquid jet by a swirling coaxial gas jet," Physics of Fluids **8**, 1696–1698 (1996).
[6] J. C. Lasheras, E. Villermaux, and E. J. Hopfinger, "Break-up and atomization of a round water jet by a high-speed annular air jet," J. Fluid Mech **357**, 351–379 (1998).
[7] J. C. Lasheras and E. J. Hopfinger, "Liquid jet instability and atomization in a coaxial gas stream," Annual Review of Fluid Mechanics **32**, 275–308 (2000).
[8] H. Eroglu, N. Chigier, and Z. Farago, "Coaxial atomizer liquid intact lengths," Physics of Fluids A: Fluid Dynamics **3**, 303–308 (1991).
[9] B. Leroux, O. Delabroy, and F. Lacas, "Experimental study of coaxial atomizers scaling. Part I: dense core zone," Atomization and Sprays **17**, 381–407 (2007).
[10] H. Zhao, H. F. Liu, X. S. Tian, J. L. Xu, W. F. Li, and K. F. Lin, "Influence of atomizer exit area ratio on the breakup morphology of coaxial air and round water jets," AIChE Journal **60**, 2335–2345 (2014).
[11] A. Kumar and S. Sahu, "Liquid jet breakup unsteadiness in a coaxial airblast atomizer," International Journal of Spray and Combustion Dynamics **10**, 211–230 (2018).
[12] A. Kumar and S. Sahu, "Optical visualization and measurement of liquid jet core in a coaxial atomizer with annular swirling air," J. Flow Visualization Image Process **25**, 229–244 (2018).
[13] N. Machicoane, G. Ricard, R. Osuna-Orozco, P. D. Huck, and A. Aliseda, "Influence of steady and oscillating swirl on the near-field spray characteristics in a two-fluid coaxial atomizer," International Journal of Multiphase Flow **129** (2020).
[14] A. Dunand, J. L. Carreau, and F. Roger, "Liquid jet breakup and atomization by annular swirling gas jet," Atomization and Sprays **15**, 223–247 (2005).
[15] Y. Hardalupas and J. H. Whitelaw, "Coaxial airblast atomizers with swirling air stream," Recent advances in spray combustion: measurements and model simulation **2**, 201–232 (1998).
[16] J. P. Matas, A. Delon, and A. Cartellier, "Shear instability of an axisymmetric air–water coaxial jet," J. Fluid Mech **843**, 575–600 (2018).
[17] A. Kumar and S. Sahu, "Large scale instabilities in coaxial air-water jets with annular air swirl," Physics of Fluids **31** (2019).

[18]I. V. Litvinov, D. K. Sharaborin, and S. I. Shtork, "Reconstructing the structural parameters of a precessing vortex by SPIV and acoustic sensors," Experiments in Fluids **60** (2019).
[19]K. Rajamanickam and B. Saptarshi, "Insights into the dynamics of conical breakdown modes in coaxial swirling flow field," J. Fluid Mech **853**, 72–110 (2018).
[20]P. Eisenklam and P. Hooper, "The flow characteristics of laminar and turbulent jets of liquid," Ministry of Supply D.G.G.W (1958).
[21]E. A. Ibrahim and S. O. Marshall, "Instability of a liquid jet of parabolic velocity profile," Chemical Engineering Journal **76**, 17–21 (2000).
[22]A. Giannadakis, K. Perrakis, and T. Panidis, "A swirling jet under the influence of a coxial flow," Experimental Thermal and Fluid Science **32**, 1548–1563 (2008).
[23]T. Ivanic, E. Foucault, and J. Pecheux, "Dynamics of swirling jet flows," Experiments in Fluids **35**, 317–324 (2003).
[24]Y. Liang, L. C. Johansen, and M. Linne, "Characteristics of sprays produced by coaxial non-swirling and swirling air-water jets with high aerodynamic Weber numbers," (2022), manuscript in preparation.
[25]S. L. Brunton and J. N. Kutz, *Data-Driven Science and Engineering: Machine Learning, Dynamical Systems, and Control* (Cambridge University Press, 2019).
[26]*FlowMaster*, Lavision (2020).
[27]K. Taira, S. L. Brunton, S. T. M. Dawson, C. W. Rowley, T. Colonius, B. J. McKeon, O. T. Schmidt, S. Gordeyev, V. Theofilis, and L. S. Ukeiley, "Modal analysis of fluid flows: an overview," American Institute of Aeronautics and Astronautics **55**, 4013–4041 (2017).
[28]G. Strang, *Introduction to Linear Algebra*, 5th ed. (Wellesley-Cambridge Press, 2016).
[29]G. Strang, *Linear Algebra and Learning from Data* (Wellesley-Cambridge press, 2019).
[30]E. Villermaux, "Mixing and spray formation in coaxial jets," Journal of Propulsion and Power **14**, 807–817 (1998).
[31]C. Dumouchel, "On the experimental investigation on primary atomization of liquid streams," Exp Fluids **45**, 371–422 (2008).
[32]D. C. Montgomery, *Design and Analysis of Experiments*, 8th ed. (John Wiley & Sons, 2013).
[33]A. Gelman, J. B. Carlin, H. S. Stern, D. B. Dunson, A. Vehtari, and D. B. Rubin, *Bayesian Data Analysis*, 3rd ed. (CRC Press, 2021).
[34]Stan Development Team, "Stan user's guide," (2022), version 2.29.
[35]Stan Development Team, "RStan: the R interface to Stan," (2020), r package version 2.21.2.
[36]M. D. Hoffman and A. Gelman, "The no-u-turn sampler: Adaptively setting path lengths in hamiltonian monte carlo," (2011).
[37]C. M. Bishop, *Pattern Recognition and Machine Learning*, 1st ed. (Springer, 2006).
[38]A. Vehtari, A. Gelman, D. Simpson, B. Carpenter, and P.-C. Bürkner, "Rank-normalization, folding, and localization: An improved r^ for assessing convergence of MCMC (with discussion)," Bayesian Analysis **16** (2021), 10.1214/20-ba1221.
[39]J. K. Kruschke, *Doing Bayesian Data Analysis*, 2nd ed. (Academic Press, 2015).
[40]Q. F. Gronau, H. Singmann, and E.-J. Wagenmakers, "bridgesampling: An R package for estimating normalizing constants," Journal of Statistical Software **92**, 1–29 (2020).
[41]Q. F. Gronau, A. Sarafoglou, D. Matzke, A. Ly, U. Boehm, M. Marsman, D. S. Leslie, J. J. Forster, E.-J. Wagenmakers, and H. Steingroever, "A tutorial on bridge sampling," arXiv (2017).
[42]H. Ge, K. Xu, and Z. Ghahramani, "Turing: a language for flexible probabilistic inference," in *International Conference on Artificial Intelligence and Statistics, AISTATS 2018, 9-11 April 2018, Playa Blanca, Lanzarote, Canary Islands, Spain* (2018) pp. 1682–1690.
[43]J. Bezanson, A. Edelman, S. Karpinski, and V. B. Shah, "Julia: A fresh approach to numerical computing," SIAM review **59**, 65–98 (2017).
[44]J. D. Hunter, "Matplotlib: A 2d graphics environment," Computing in Science & Engineering **9**, 90–95 (2007).